UNIVERSITÀ DEGLI STUDI DI PADOVA

DIPARTIMENTO DI INGENERIA INDUSTRIALE DII

CORSO DI LAUREA IN INGEGNERIA DELL'ENERGIA ELETTRICA

STUDIO SPERIMENTALE E CON MODELLI NUMERICI DEL SISTEMA G1 INSTALLATO NEL FORNO *i*DSS

Relatore: Dott. Ing. MICHELE FORZAN
Candidato: SIMONE TURETTA

ANNO ACCADEMICO 2016-2017

"Sai cosa dicono del gioco del calcio?
Che è un gioco da gentiluomini giocato da selvaggi."

Contents

List of Figures

List of Tables

Abstract

The main aim of this thesis is the numerical and experimental analysis on a furnace suitable for an innovative process for the recycle of Silicon by induction heating, this activity is supported by the European project called SiKELOR. The goal of this project is to create a system for the recycle of Silicon coming from the waste of wafer production and obtain an high quality product.

The document starts with the description of two principal solidification process typologies. Then my thesis presents a comparison between two types of experimental furnaces realized by University of Padova. The first one is the so called "G2.5" that was used for a first analysis and tests of the process and "G1" that is the new configuration of the furnace used in LEP. After, the results of a FEM analysis of G1 furnace will be shown. These simulations were done in order to looking for some behaviours not considered in the design process and to help the step-by-step assembly of the real furnace's components. At the end, there is a comparison between FEM analysis and experimental tests done on the furnace in order to asses the numerical models.

Sommario

Lo scopo principale di questa tesi è l'analisi numerica e sperimentale di un forno innovativo per il processo di riciclo degli scarti di Silicio provenienti dalla produzione dei wafer. Questa ricerca è supportata dal progetto Europeo denominato SiKELOR.

La prima parte della tesi si concentrerà sulla descrizione dei processi di solidificazione del Silicio. In particolare, verranno esposti i metodi per la produzione del silicio monocristallino e policristallino. Della prima categoria si tratteranno il processo Czochralski e il metodo Float-Zone. Della seconda, invece, viene trattato il processo Direct Solidification; questo metodo è anche quello implementato sul forno. Questa parte si conclude con la descrizione delle parti principali del forno G2.5, precedentemente installato nel laboratorio, e la sua nuova versione: il G1. Le due versioni si differenziano l'una dall'altra per delle modifiche che riguardano essenzialmente: la dimensione del lingotto e dell'induttore laterale.

Nella seconda parte della tesi vengono mostrati i risultati delle simulazioni agli elementi finiti. Questa analisi FEM è stata eseguita per capire il funzionamento delle parti principali del forno G1. Verranno esposti i risultati di simulazioni elettromagnetiche ed, infine, di simulazioni che vedono l'accoppiamento anche del problema termico. Questa analisi evidenzierà il malfunzionamento di una nuova parte che è stata inserita nella configurazione G1. Da questo punto in poi, l'attenzione si concentrerà su questo problema e la sua soluzione.

La terza parte tratterà il problema evidenziato nella sezione precedente. In particolare, verranno esposte varie soluzioni le quali saranno poi confrontate. Dal confronto delle varie nuove configurazioni ne uscirà quella da implementare nel forno reale.

Infine, ci sarà una sezione dove verrà mostrato il confronto tra prove sperimentali ed analisi al calcolatore. Questo confronto è utilizzato per verificare la bontà del modello FEM realizzato e per capire se i risultati ottenuti nelle simulazioni potranno essere in linea con quelli sperimentali.

Chapter 1

SiKELOR, FP7-Eu Project Description

Silicon is the material of choice for the fast growing solar market because it converts solar energy into electric power in a relatively efficient manner. Many studies are done in order to understand how manage the production of this important material in a better way, and SiKELOR is one of these.

1.1 Solidification processes

There are many typologies of processes with the goal of Silicon production used with industrial applications. In fact, solar cells are mainly manufactured using SC[1] and MC[2] Silicon wafers. SC Silicon, produced by processes like Czochralski or Float-Zone, is used in the manufacture of solar cells and electronics components. Instead, MC Silicon, produced by DS process, is used only for solar cells.

1.1.1 Czochralski Method

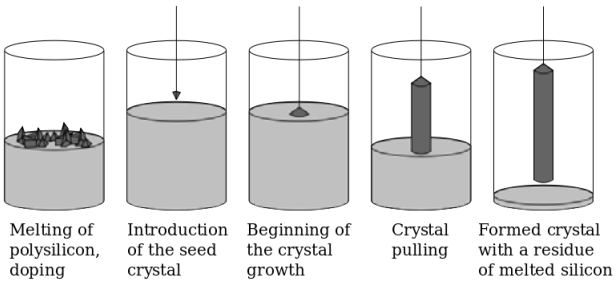

fig. 1.1: CZ process simplify steps

[1] SC: Single Crystalline
[2] MC: Multy Crystalline

Polish scientist Jan Czochralzki invented the method in 1915 while investigating the crystallization rates of metal.

The CZ[3] process creates a high-purity mono-crystalline Silicon that is melted in a Quartz crucible at $1425°C$ in Argon atmosphere. A rod-mounted seed is dipped into the molten Silicon, then is slowly pulled upwards and rotated simultaneously like in fig. 1.2. In this way it is possible to create a large cylindrical ingot up to 300 mm of diameter.

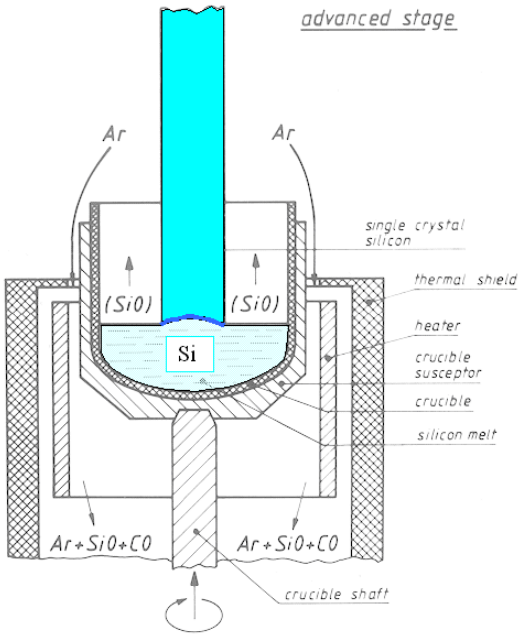

fig. 1.2: CZ furnace structure

Crucible and seed, usually, rotate in opposite direction. The immersed part of the crystal seed into the molten Silicon melts itself but the outer part is still solid. During the process of lifting-rotation the molten Silicon gradually solidifies at the interface between crystal seed and the molten Silicon, so a large mono-crystalline is created. In particular, the molten Silicon atoms which touch the mono-crystalline seed solidify quickly adhering to the seed and are oriented according to the Silicon structure, so also them produce a mono-crystalline lattice.

The control of molten Silicon temperature, of atmosphere in the chamber, of rotation speed, of lifting speed and of vibration absence allow to produce perfect cylindrical ingots of high purity Silicon. The process lasts some days in order to produce ingots of 1 meter length up to 300 mm of diameter.

[3]CZ= Czochralzki

1.1.2 Float-Zone Method

Like Czochralski process, the float-zone method realizes the growth of a high-purity crystal. The procedure consists on the movement of a poly-crystalline Silicon bar in vertical position that rotate simultaneously, trough an inductor. This inductor melt the Silicon from bottom to top starting from a crystal seed that begin the crystallization. Impurities will be segregated in the melted zone like in fig. 1.3, in this way the solid Silicon is purified. This procedure is repeated many times along the bar in order to obtain an ingot of pure Silicon crystal.

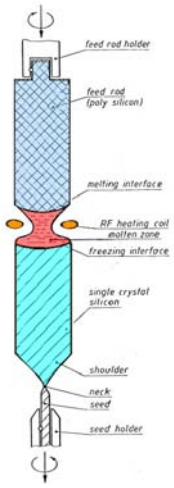

fig. 1.3: Float Zone Method

1.1.3 Directional Solidification Method

The process called Directional Solidification allows to produce a poly-crystalline Silicon, it gathers many strategies to obtaining a directional thermal flux. The differences between these techniques consist in the method for establishing the temperature gradient that causes the solidification and determines the crystalline structure. Some of these techniques are:

- Bridgman Technique: the thermal gradient is created by moving the crucible, usually downward;
- HEM[4]: in this case, thermal flux is created by cooling the crucible bottom;
- VGF[5]: this method includes several controlled warmer placed conveniently around the crucible to obtain a thermal gradient.

[4]HEM: Heat Exchanger Method
[5]VGF:Vertical Gradient Freeze

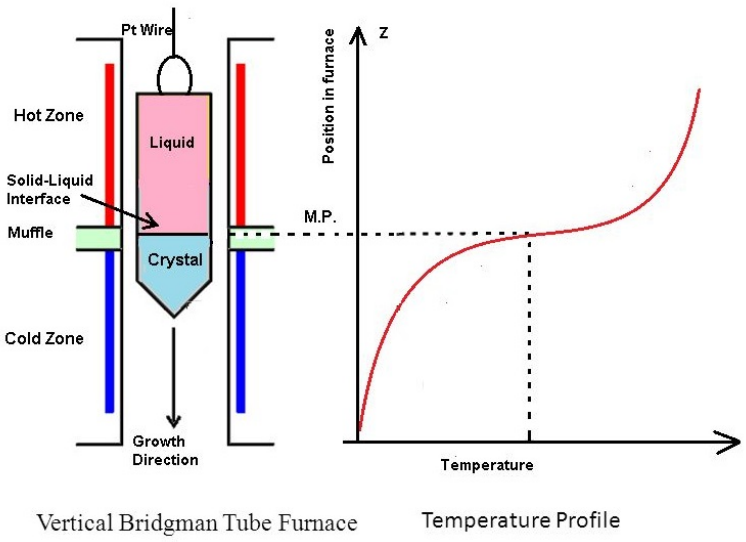

fig. 1.4: Bridgman Technique

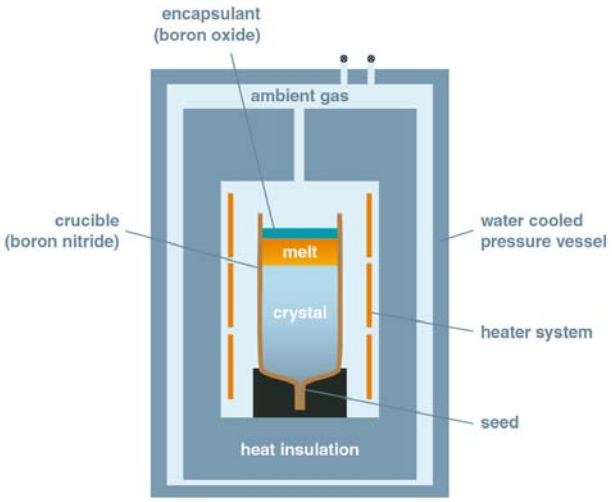

fig. 1.5: VGF Technique

In a DS furnace, the Silicon feedstock, usually in chunks of poly-crystalline material with dimensions of few centimetres, is loaded in a Quartz (SiO_2) crucible coated by Silicon Nitrite (Si_3N_4) in order to prevent the sticking of molten Silicon to the crucible and SiO_2 diffusion during the cooling process. Due to the high temperature reached by the crucible it assumes a plastic behaviour, so a mechanical support is needed. This support, usually, is made by isostatic graphite. The crucible is disposable because it reaches the mechanical break, in order to avoid this problem some reusable crucibles

are developing, but they are not used in industrial application.

A further classification for DS furnace is based on the crucible internal side length. This classification is called Generation (G). The crucible internal side must have dimension of a standard PV cell multiple added by $25 - 30mm$ considered the scrap caused by the diffusion of SiO_2 in the outer part of Silicon. For example, the G5 crucible has dimension of $84 \times 84 \times 26cm^3$, so it's possible to obtain $5x5$ bricks. For improving the process performance and its cheapness, bigger crucibles have been developed. Greater dimensions guarantee the process cheapness because of:

1. The increasing quantity of Silicon product per furnace;
2. The increasing efficiency of the process due to the decrease of the ratio thermal losses over Silicon quantity.

Now, for the principal furnace producer (ALD, ECM, GT-advance, JYT) the state of the art is a G6 configuration that is able to handle ingots of $1000 \times 1000 \times 429mm^3$ and a weight of about $1000kg$. But there is a limit for ingots size, in fact a further dimension increase could enlarge also the final costs of the system due to more expensive technical solutions in comparison with the decreasing business cost.

1.2 Electromagnetic Stirring

The principal problem about the crystallization of molten material concerns the formation of convective flow and turbulence in the melt. These effects product huge variation in crystal growth rate that allows a non homogeneous composition. During CZ process, as said before, the melt movement is obtained by the simultaneously rotation in opposite directions of crucible and crystal seed; trough the stirring process this effect is obtained by the EMFs[6] acting on the melt.

From the beginning of electromagnetic stirring this processes used SMF[7], whereas now the development of techniques using NSMF[8] allows the harmonisation of convective flows inside the melt in a more efficient way. In fact, NSMFs compared to SMFs have a better interaction with the melt, this quality is defined by the ratio between the EMFs inducted and the buoyancy forces. Regarding NSMF is possible to say:

[6]EMF: Electro Magnetic Force
[7]SMF: Stationary Magnetic Field
[8]NSMF: Non Stationary Magnetic Field

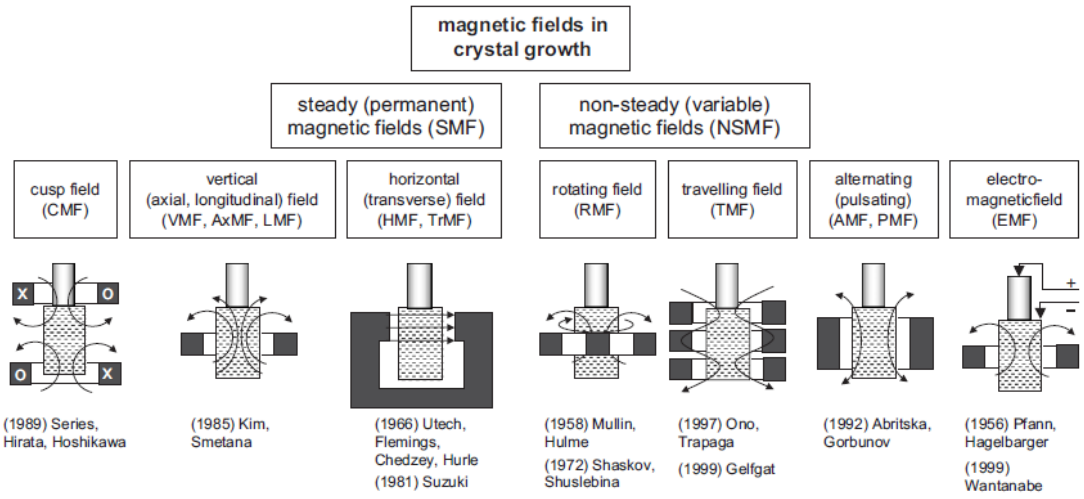

fig. 1.6: An overview on stirring techniques

- RMFs[9] allow the increase of melt mixing controllability. This kind of magnetic field can be produced by a machine like that one in fig. 1.8.

- AMFs[10] and TMFs[11] created by an inductor like that one in fig. 1.9 allow, instead, a direct action on the diffusion boundary layer, on Marangoni flows and on the curvature of solidification front. In particular, using TMFs an axisymmetric Lorentz force field is produced that has the same morphology of buoyancy force field.

So, in order to obtain high quality Silicon, an optimal crystal lattice is needed. For SiKELOR project, the field configuration chosen for electromagnetic stirring is TMF. Historically, for industrial applications, RMF are used for keep in rotation molten materials during continuous casting processes like lamination or extrusion, for example, of steel or aluminium.

Regarding TMF, the conventional configuration used for supply the inductor is a three-phase current at $50Hz$ system with a delta connection. But it's possible to use a star connection of the three coils in order to supply each of these separately with different currents, frequencies and phase shifts. This flexibility is useful for adapting the stirring process to every situation that could be present during the solidification process of Silicon.

[9] RMF: Rotating Magnetic Field
[10] AMF: Alternating (pulsating) Magnetic Field
[11] TMF: Travelling Magnetic Field

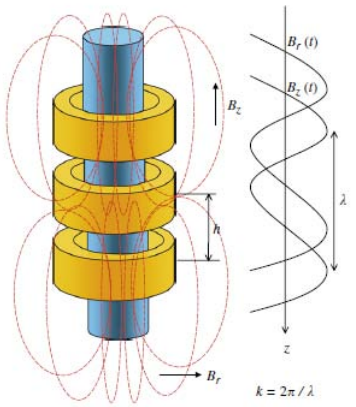

fig. 1.7: An example of travelling magnetic field

fig. 1.8: An example of rotating stirrer

fig. 1.9: An example of linear stirrer: *i*DSS lateral inductor

1.3 SiKELOR Project

The European project SiKELOR[12] proposes a Silicon waste recycling process able to produce high quality MC-Si ingots from the kerfs resulting from mainly the wafer manufacturing. This typology of process is called Mono-Like-Casting. In particular project SiKELOR consists in the modification of a DS furnace with the insertion of induction heating, at industry level graphite resistors are used, and stirring process in order to obtain a more qualitative final product. The directional solidification system uses a technique in order to create the temperature gradient inside the Silicon, in SiKELOR particular case the HEM technique is implemented. In addition to the lateral inductor that is used for both heating and stirring, heating is provided with two pancake inductors, one on the furnace top and one on the furnace bottom. These two inductors will be controlled in order to create the temperature gradient that allows the correct Silicon solidification. In particular the bottom inductor will provide, in addition to heating, also the cooling to establish the required temperature gradient.

The research activities are focused on all process steps as compaction, melting, purification and casting. Four main goals are defined:

1. Improving the thickening of dry Silicon powder without the insertion of contaminations.

2. Fusion and purification of Silicon with electromagnetic separation.

3. Casting of poly-crystalline Silicon ingots using DS.

4. Prove the process cheapness

Then, the new process is named *i*DSS that stay for Induction Directional Solidification System.

The project performs a combination of numerical simulation, physical modelling, and demonstration experiments.

The University of Padua, in particular LEP[13] contributes to the SiKELOR project with numerical simulation, design of mechanical parts and with experimental tests on the *i*DSS furnace.

[12] SiKELOR: Silicon KErf LOss Recycling
[13] LEP: Laboratorio di Elettrotermia di Padova

Chapter 2

G2.5: the starting model

This chapter includes a short overview of the previous furnace G2.5 used for real tests in LEP. Principally will be exposed the furnace parts and the differences in comparison with G1 configuration.

2.1 Process description

First of all, the process steps are shown (fig. 2.1) for understanding how furnace works.

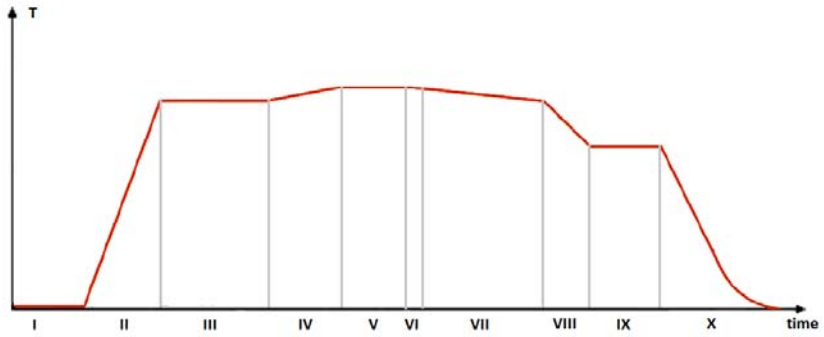

fig. 2.1: DS process steps

1. **Cleaning**: for removing the impurities present in the air a cycle of vacuum is done. First, inside the furnace it is reached a pressure of $0.005 - 0.5mbar$. After, a inert gas, such as Argon or Helium, is pumped inside the furnace until pressure reaches a value of $0.02 - 0.1mbar$.

2. **Heating**: the overall system is heated until Silicon reaches the fusion temperature. A certain heating rate is imposed, it prevents the structure breaks due to the high thermal stress.

3. **Fusion**: in this heating phase, the heat is absorbed only by the Silicon. The accumulate heat corresponds with the latent heat of fusion, it is needed for the state change of the material, so the temperature does not change.

4. **Overheating**: for creating the correct thermal gradient in the molten Silicon is necessary to exceed the fusion temperature.

5. **Conservation**: this step is useful for removing the residual solid Silicon.

6. **Vertical thermal gradient**: before the solidification process, a vertical thermal gradient is created by cooling down the furnace bottom. In the upper part, the system continues to heat the Silicon.

7. **Solidification**: in response to the vertical thermal gradient the temperature starts to decrease. When melt temperature decreases under fusion value, the solidification starts. Solidification rate is $0.6 - 25mm/h$, it is obtained controlling the thermal gradient.

8. **Cooling**: the system is cooling down until a certain temperature, useful for the annealing process, is reached.

9. **Annealing**: in order to simplify the phenomena of diffusion and stress release, the Silicon needs an homogenization step.

10. **Final cooling**: the furnace is brought to the room temperature with a controlled cooling process. This process prevents the formation of too high stress forces inside the Silicon.

2.2 Furnace description

The overall furnace is shown in fig. 2.2. Now, the principal parts of this configuration are presented.

2.2.1 Upper and Lower inductors

The inductors placed on the top and bottom part of the furnace are of the type of pancake. As said before, these inductors are used to create the vertical thermal gradient.

fig. 2.2: G2.5 inside: inductor and monolith box

The upper pancake (fig. 2.3(b)) has circular cross section. Whereas, the lower pancake inductor (fig. 2.3(a)) has rectangular cross section in order to increase its exchange surface. This trick is useful for controlling in a better way the imposition of thermal gradient on Silicon.

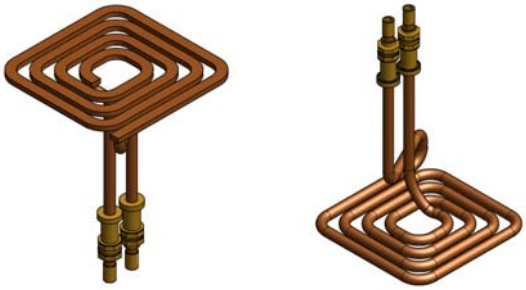

(a) Phase 0° (b) Phase 120°

fig. 2.3: Upper and lower pancake inductors of G2.5 configuration

2.2.2 Lateral inductor

The lateral inductor (fig. 2.4) is composed by six coils, with circular cross section, connected in series and it surrounds the entire crucible.

2.2.3 Vessel and insulators

In order to limit the thermal losses of melt, the vessel is surrounded by insulators. The material used for insulating the vessel is isostatic Graphite. The insulator's structure

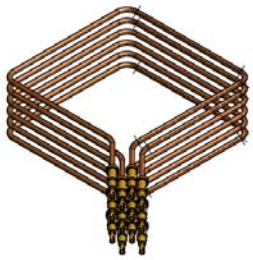

fig. 2.4: Lateral inductor of G2.5 configuration

is the monolith shown in fig. 2.5.

fig. 2.5: Graphite box of G2.5 configuration

2.3 Differences between G2.5 and G1

With G1 configuration we want to get a better quality of the final product. For doing this, higher magnetic field is needed for heating and stirring processes. To simplify the system, crucible's dimensions are decrease. This decision makes necessary the change of lateral inductor and monolith in Graphite that surrounds the crucible.

1. **Lateral inductor**
   New lateral inductor is composed by 3 independent groups of coils. This configuration permits to create in a more easy way the double frequency supply. Moreover, the new inductor has narrower coils and doubling in number respect G2.5 furnace. So, it creates an higher magnetic field, then the effects on silicon are more intense.

2. **Graphite box**
   The monolith in Graphite is substituted by a box of "cement-like" material (fig. 2.6)

because the dimensions decrease. The monolith had, also, the purpose of to sustain the upper susceptor. With this aim, a new AISI-304 structure is built up. It is fixed directly to the furnace's wall by four brackets. Actually, due to the high temperature reached by the susceptor, an Aluminium oxide support is placed between Graphite and steel structure.

fig. 2.6: New crucible's box

3. **Resonant converter**
   The change of lateral inductor needs, also, the change of the converter that supply the double frequency current. The new converter was installed on the furnace by EAAT, a partner of SiKELOR project. For characterize it some experimental test are done.

Chapter 3

Numerical Analysis of G1 furnace

The induction heating and stirring processes work at different values of frequency and current. The stirring process works with a three-phase current at some terms of Hertz, e.g. $50Hz$, of about $2kA$, instead the induction heating process works with a single-phase current of about $1kA$ at $4kHz$. Actually lateral inductor is supplied by a series resonant converter so the values of frequency and current for both processes depend on the values of inductance and resistance "view" by the converter. So we can consider the previous values of frequency and current as reference values only for simulations, since in reality some small differences are expected Furthermore, it is possible to study the overall behaviour of the furnace by applying the superposition of effects, due to the linearity of the numerical problem.

3.1 Steady State AC Magnetic Model: Stirring Analysis

3.1.1 Geometry

The geometry of first considered model is shown in fig. 3.1. In this model we can identify: molten Silicon, lateral inductor composed by three groups of four Copper tubes, the AISI-304 structure, Aluminium oxide support and the upper susceptor in Graphite. Two tetrahedron, invisible in fig. 3.1, are built between the lateral inductor and the steel structure in order to relax the mesh faster; in that position, without this trick, we could have a too dense mesh that gets slower the solving process. Hereinafter, for stirring analysis, on figures Aluminium oxide support and Graphite pieces are setted invisible in order to simplify the view.

Only a quarter of the real furnace is modelled for decrease the computational costs of

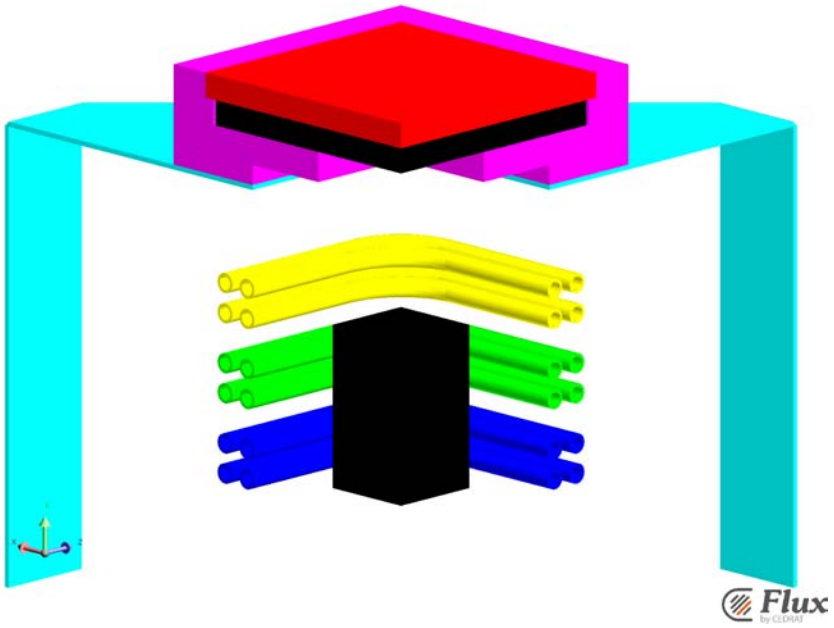

fig. 3.1: Geometry of $1/4$ model

simulations. Two symmetries are created with boundary conditions of tangent magnetic field (the current flows trough the symmetry plane). But, these symmetries do not permit the analysis of electric terminal of the lateral inductor.

In order to limit the calculus domain, a parallelepiped infinite box is created. It has to contain the field's lines without perturb them. In this model the magnetic field is concentrated only in its centre so it is possible to build the infinite box only a little bit bigger than model.

3.1.2 Materials

Materials used in this model are: isostatic Graphite for susceptor, felt graphite for insulating, Aluminium oxide for susceptor support, AISI-304 for structure that hold up the previously parts, Copper for inductor and, obviously, molten Silicon. The electromagnetic properties of these materials are shown in tab. 3.1.

For simplify the models and make the simulations easier, each material is considered isotropic and linear. This hypothesis is in agreement with the real model especially with the materials permeability. Otherwise in case of carbon steel a non linear model is needed due the saturation behaviour of the B-H curve, in fact it is angular coefficient responds to the relative permeability. The felt Graphite, using for cover the upper susceptor, has an anisotropic resistivity. But, its anisotropy makes it an insulator.

tab. 3.1: Electromagnetic properties of materials

	Resistivity $[\Omega m]$	Permeability $[/]$
Isostatic Graphite	1925×10^{-8}	1
Felt Graphite	Insulator	1
Aluminium oxide	Insulator	1
AISI-304	120×10^{-8}	1.008
Copper	1.564×10^{-8}	1
Silicon (molten)	0.7×10^{-8}	1

3.1.3 Physics

The principal point of this section is understanding how model lateral inductor. In particular it is possible to choose between:

- **Solid conductor**
  This configuration assumes a non-uniform distribution of current density inside the volume. This approach permits the user to control the solid conductor with a circuit or to not control it and leave the command to physics. So, in this case, the control occurs with a current imposition. The positive feature is that an automatically calculus of electrical parameters, such as resistance or voltage, can be done. This configuration also allows to understand the real current density distribution inside the conductor, this is an important simulation object, for example, in case of steel hardening. So the results depend from mesh size: tinier the mesh more precise the results but this means higher computational costs.

- **Coil conductor**
  This second configuration assumes an uniform distribution of current density inside the volume so it means a priori knowledge of this feature. In opposition of solid conductor, with this method it is possible to build up a coarser mesh in order to decrease computational costs, but it is impossible to evaluate electrical parameters. This method forces the user to control the conductor with a circuit or with an imposing current so it is impossible to evaluate the eddy currents in it.

To prove the uniform current density distribution inside an inductor is important to evaluate the skin depth with eq.3.1.

$$\delta = \sqrt{\frac{\rho}{\pi f \mu_r \mu_0}} \tag{3.1}$$

If conductor thickness is smaller than skin depth, the hypothesis of uniform current density is verified. If skin depth doesn't fulfil this hypothesis, a rule suggests to divide the skin depth at least in four or five mesh elements. In this case the skin depths of the material used, for the stirring frequency of about $50Hz$ are, obviously, bigger than the inductor and steel support thickness. Based on this consideration and on characteristics of both configurations, to each coil of lateral inductor is associated a coil conductor with an imposed current. Otherwise, molten Silicon and steel structure are modelled with a solid conductor so it is possible to evaluate eddy currents.

3.1.4 Mesh

Geometry is built up by applying several transformations for obtaining lines from the extrusion of points, faces from lines and volumes from faces. This method allows Flux to build faster a better mesh. Furthermore, for hexahedral volumes a mapped mesh is built up. This expedient permits to improve the interpolation's precision inside the volumes without second order elements and computational cost increase. Notably a mapped mesh is possible to build only on six faces volumes. Mesh line tool is used for meshing the model, in order to control elements size. The mesh on faces is shown after in fig. 3.2.

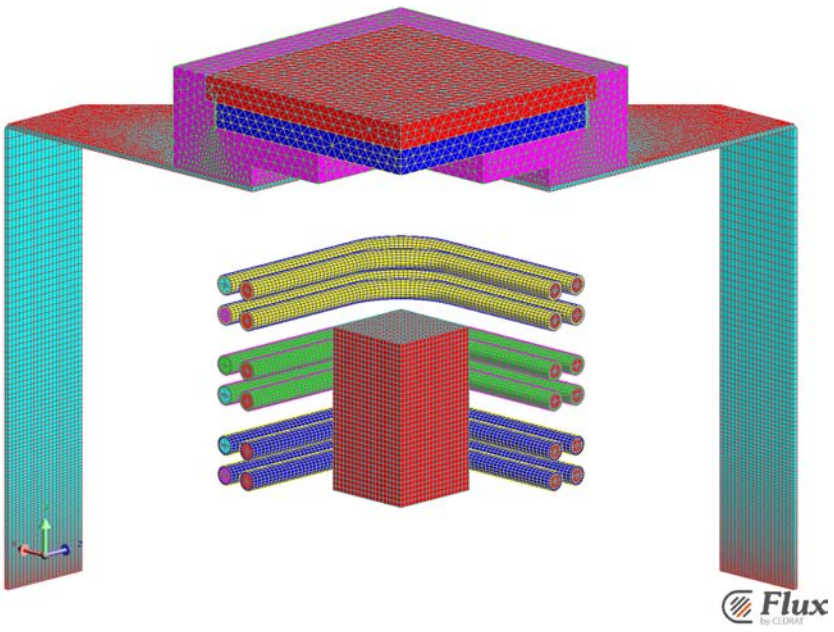

fig. 3.2: Mesh of $1/4$ model

The mesh algorithm creates approximately 1.8 millions of volume elements and 380 thousands nodes.

All models are solved using $\boldsymbol{A}V$ formulation for evaluating in a better way Joule losses. In fact, Joule losses are calculated by the integration of power density ρJ^2 on the volumes and current density J is strictly connected with the Magnetic Vector Potential $\boldsymbol{A}$.

3.1.5 Results and Post Processing

The principal purpose of this analysis is to understand how the Lorentz forces act on the molten Silicon, them are evaluated by eq.3.2 like a density of force.

$$\boldsymbol{F} = \boldsymbol{A} \times \boldsymbol{B} \quad [\frac{N}{m^3}] \tag{3.2}$$

It is possible to write these forces also in another way like in eq.3.3.

$$\boldsymbol{F} = \boldsymbol{J} \times \boldsymbol{B} = \boldsymbol{J}_{Re} \times \boldsymbol{B}_{Re} \cos^2 \omega t + \boldsymbol{J}_{Imm} \times \boldsymbol{B}_{Imm} \sin^2 \omega t - (\boldsymbol{J}_{Re} \times \boldsymbol{B}_{Imm} + \boldsymbol{J}_{Imm} \times \boldsymbol{B}_{Re}) \frac{\sin 2\omega t}{2} \tag{3.3}$$

So, the Lorentz forces are made up by two components. The first component has an integral on its period different to zero, then it works like an "offset". The second component has double frequency respect the current, so it needs an analysis on the period.

Lorentz force are connected to another typology of force called "Leenov-Kolin". Leenov and Kolin had calculates the forces those act on a spheric particle suspended into a molten metal. The eq.3.4 is valid only in the case of different electrical conductivity of particle and metal.

$$\boldsymbol{Fp} = -\frac{3}{2}\frac{\sigma_l - \sigma_p}{2\sigma_l + \sigma_p} V_p \boldsymbol{F} \quad [N] \tag{3.4}$$

In eq.3.4 $\sigma_p[S/m]$ and $\sigma_l[S/m]$ are, respectively, the particle and liquid conductivity, V_p is the particle volume and F is the Lorentz force. Usually $\sigma_p << \sigma_p$, so it is possible to simplify the relation to eq.3.5 where the particle's volume is extended.

$$\boldsymbol{Fp} = -\frac{3}{4}\frac{\pi d_p^3}{6} \boldsymbol{F} \quad [N] \tag{3.5}$$

For understanding the forces behaviour showed in fig. 3.6, magnetic field, produced by the lateral inductor, and eddy currents inside molten Silicon are shown.

As said before, the travelling magnetic field, showed in fig. 3.3, is produced by a three-phase supply so it changes with phase angle. In particular, the maximum magnetic field is located on the phase that has the maximum current real part. In order to see its

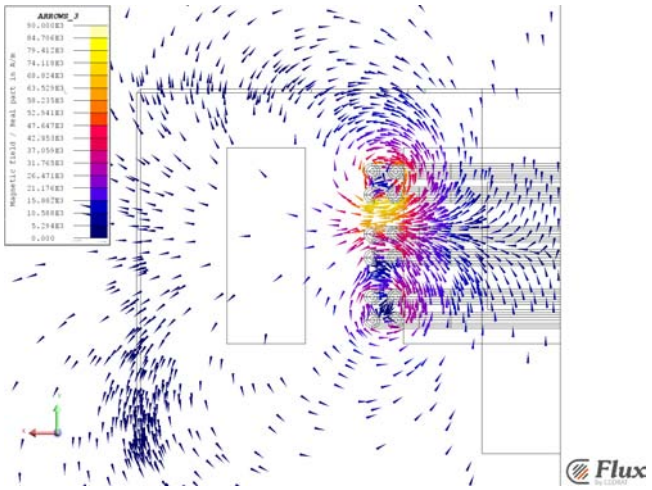

fig. 3.3: Magnetic field at 0 degree

behaviour at different phase angle the fig. 3.4(b) and fig. 3.4(c) are proposed.

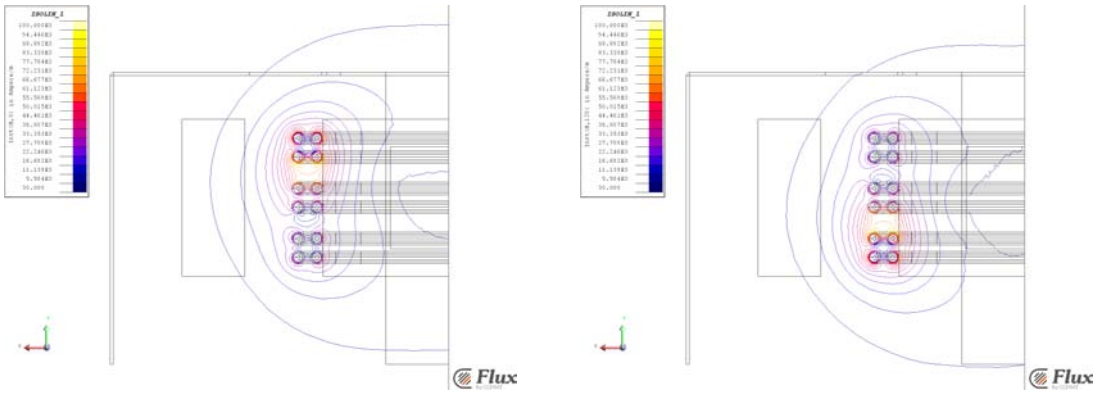

(a) Phase 0°

(b) Phase 120°

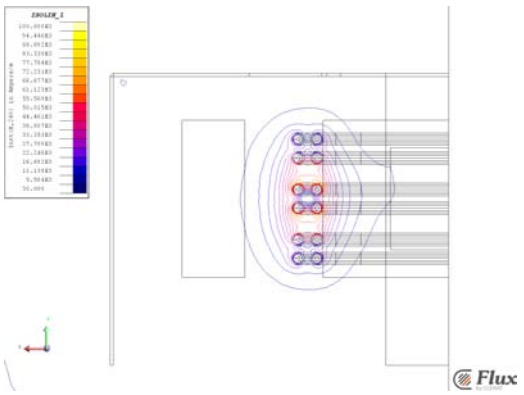

(c) Phase 240°

fig. 3.4: Magnetic field for stirring process

In fig. 3.5, current density distribution inside the molten Silicon is showed. Eddy current distribution, magnetic field and so magnetic flux density are concentrated on

the edges of molten Silicon; then in these zones there are the grater magnetic forces. Based on formula 3.3, forces have a frequency of $100Hz$. Furthermore, forces behaviour changes on its period and it is useful to see it at different phases like in fig. 3.6. Based on the previously considerations, in order to have greater Leenov-Kolin forces, is necessary that liquid motion brings the particles on crucible walls. In this way, it is possible to obtain a good segregation of impurities.

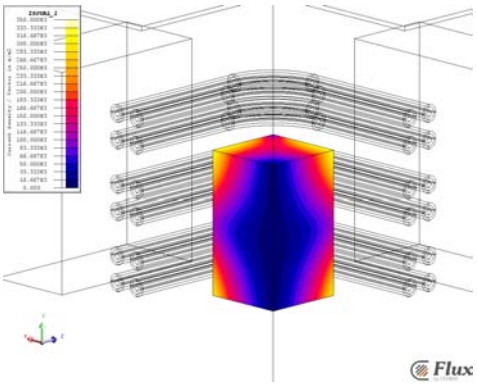

fig. 3.5: Current density distribution inside molten Silicon

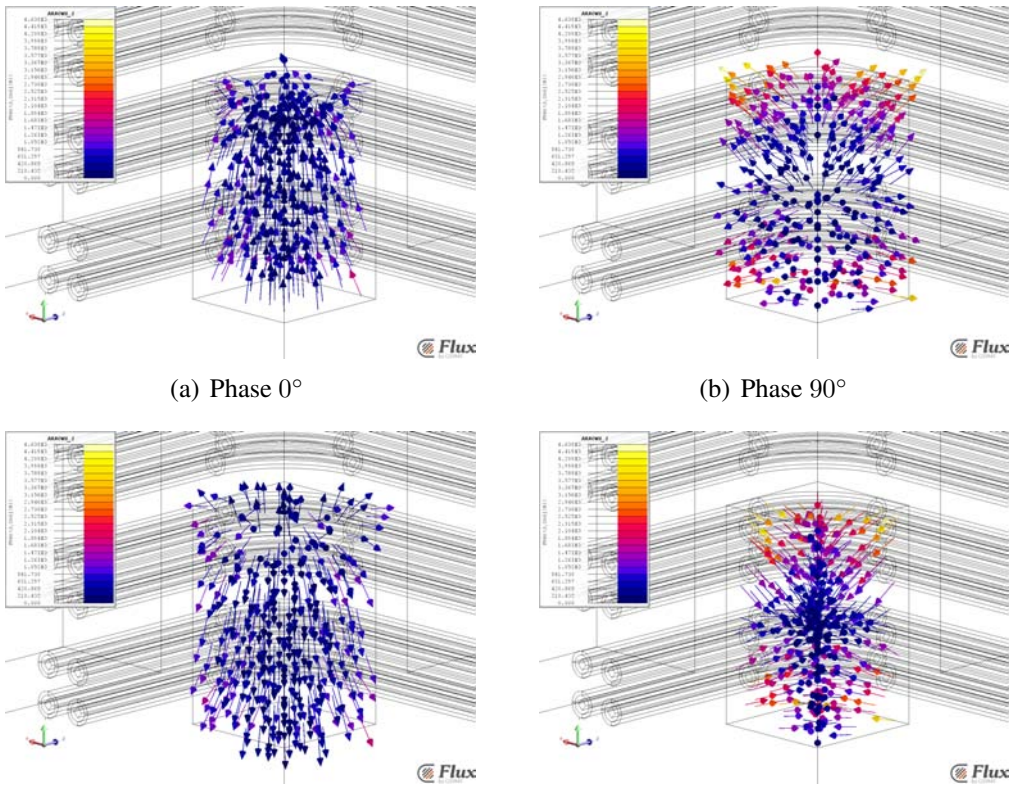

(a) Phase 0° (b) Phase 90°

(c) Phase 180° (d) Phase 270°

fig. 3.6: Forces acting in molten Silicon

In fig. 3.6, is clear how these forces work: for the phase from 0 to 180 degrees the

forces constrict liquid, for the other 180 degrees they act, on the contrary, expanding molten Silicon. Therefore, the maximum forces in absolute value acting on the liquid take place at $90°$ and $270°$ respectively in expansion and compression. These forces combined with the buoyancy effect and Marangoni forces determines the hydrodynamic motion of the molten Silicon.

This simulation draws to attention the fact that stirring process doesn't feel the effect of steel structure and vice versa: in fact the Joule losses computed inside the AISI-304 region are $26W$.

3.2 Steady State AC Magnetic Model: "cold" Heating Analysis

The successive step is analysing the behaviour of steel structure in respect with the induction heating process using the lateral inductor. This simulation is called "cold" because the materials resistivity is referred to the room temperature. Geometry and mesh used for this simulation are the same used for the stirring process analysis. About physics the main differences are associated to the current imposed in coil conductors, as said before in this case a single-phase current of $1kA$ at $4kHz$ is used.

Just like the previously model, skin depths are evaluated by eq.3.1 in order to understand if is needed a change of mesh:

tab. 3.2: Skin depths at $4kHz$

	Resistivity $[\Omega m]$	Relative Permeability $[/]$	Frequency $[Hz]$	Vacuum Permeability $[H/m]$	δ $[mm]$
Copper	1.564×10^{-8}	1	4000	$4\pi \times 10^{-7}$	0.995
AISI-304	120×10^{-8}	1.008			8.68
Silicon	0.7×10^{-8}	1			0.666
Graphite	1925×10^{-8}	1			34.9

Actually, the mesh of previous model was build up knowing the skin depths at $4kHz$.

3.2.1 Results and Post Processing

The first entity to analyse is the magnetic field produced by lateral inductor and how it concatenates the steel structure, that is the principal object of this study.

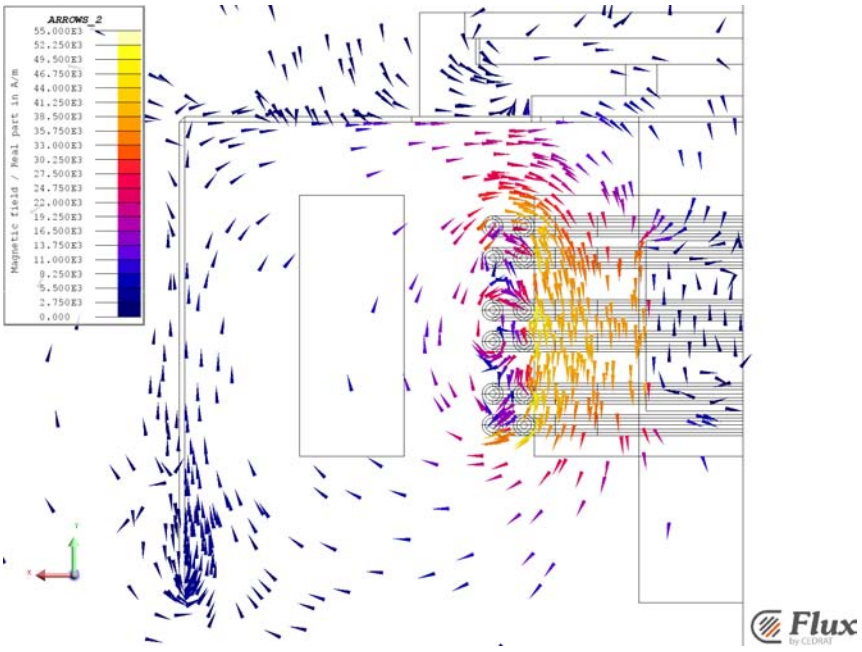

fig. 3.7: Single-phase heating magnetic field

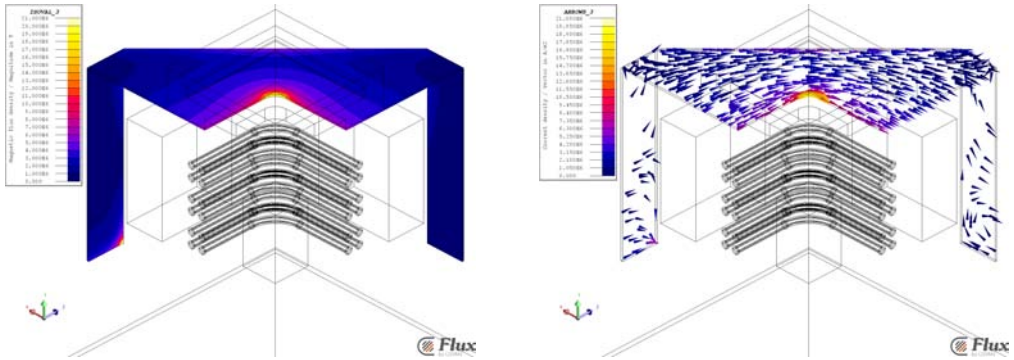

(a) Isovalues (b) Arrows

fig. 3.8: Eddy current on steel structure in "cold" analysis

The magnetic field produced by lateral inductor concatenates the steel structure essentially in the horizontal part, because of short distance between them. Moreover, the hole placed in steel structure's flat part is smaller than the hole described by the lateral inductor, so stronger magnetic field is concatenated in this part. The behaviour of eddy currents inside the steel structure is showed in fig. 3.8.

The fig. 3.8(b) shows eddy currents path on the flat surface. As we can see, the critical part is the hole contour, in particular current density increases on the edges. Vertical parts of the steel structure, called "legs", are almost not affected by the magnetic field so there are not strong eddy currents. On the bottom part of the left leg seems to be a huge current density caused by the magnetic field interaction with the steel. Actually

this current density doesn't seem to has reason to exist because there is not magnetic field concatenated with that part. So, tinier mesh is built on the bottom part of both legs in order to understand phenomena, but the problem persists. In fig. 3.8(b), it seems to be a current "well" in the above-mentioned region because the arrows converge there. But, yet again, there is not any physical meaning for this behaviour. Starting from here, to this leg is supposed a behaviour same as the right leg, in particular the same Joule losses are imposed.

Upper susceptor's eddy currents (fig. 3.9) have the same path of the currents on steel structure's flat part, but with lower intensity. This behaviour is due to the increase of distance from the inductor to the scuscpetor and to the shield effect consequence to the steel's eddy currents.

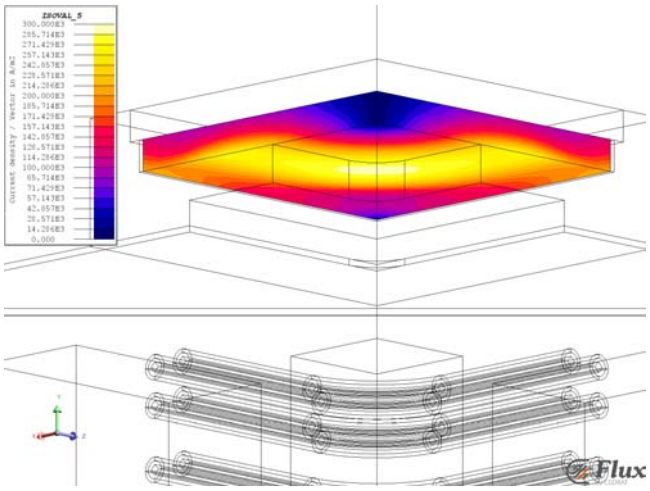

fig. 3.9: Current density distribution on upper susceptor

These current density distributions, in particular on the steel structure, lead to Joule losses that are summarized in tab. 3.3.

tab. 3.3: Joule losses "cold" model

Flat part $[W]$	Right leg $[W]$	Left leg $[W]$	Overall $[W]$	Silicon $[W]$
2965	57	540	3079	2790

These values are calculated by integration on the volumes of the model, so these Joule losses concern only a quarter of the actual furnace.

Based on the values resumed in the table, total losses, refer at the entire model, are of about $12kW$. This is an alarming value, not only for process efficiency, but also for temperature that the steel structure could reach.

3.3 Steady State AC Magnetic Model: "hot" Heating Analysis

For building a model closer to the reality, materials' resistivity are modified taking into account the temperature, that each part can reach during the process. In particular these considerations were done:

- Lateral inductor's coils consist of a Copper tube with an external diameter of $23mm$ and internal of $20mm$, in order to cooling down the coil pumping cold water inside it. This is necessary to avoid a too high temperature achievement. So, coils temperature supposed is $50°C$.
- From experiments lead on the G2.5 furnace the temperature measured on the upper susceptor was about $1600°C$, so the resistivity of Graphite refers to this temperature.
- Molten Silicon supposed already a higher temperature than $1414°C$, so resistivity remains the same.
- The temperature reached by steel structure is unknown now and it is supposed near $700°C$ that is the maximum temperature reachable by the AISI-304 without a mechanical properties worsening.

In conclusion, the imposed resistivity are resumed in tab. 3.4.

tab. 3.4: Materials' resistivity of hot models

	Resistivity $[\Omega m]$
Isostatic Graphite	1925×10^{-8}
Felt Graohite	Insulator
Aluminium oxide	Insulator
AISI-304	120×10^{-8}
Copper	1.564×10^{-8}
Silicon (molten)	0.7×10^{-8}

3.3.1 Results and Post Processing

The magnetic field and eddy currents distribution evaluated in this model are the same of previous simulations, because of same current imposed on lateral inductor. The

differences are referred to the intensity of eddy currents and then to the Joule losses.

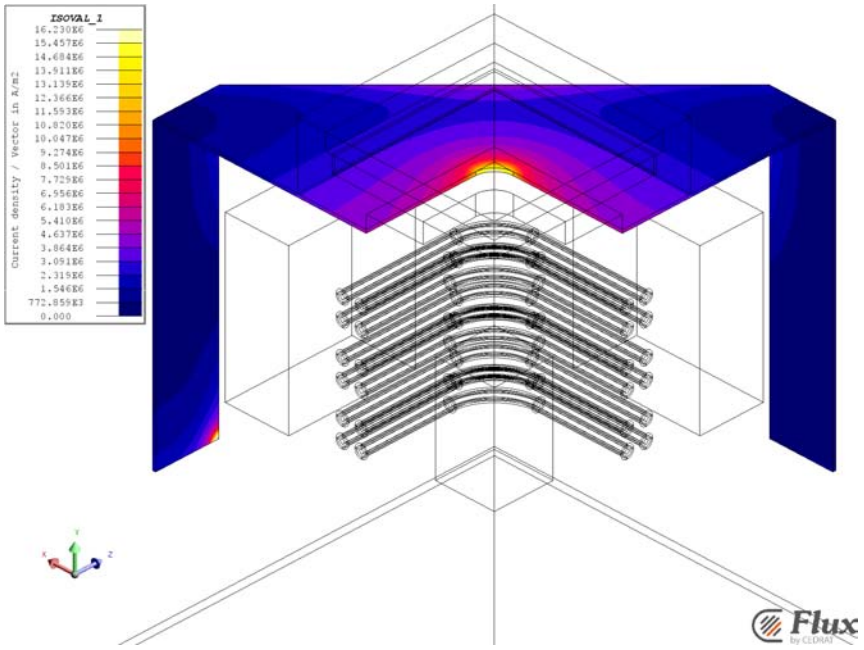

fig. 3.10: Eddy current on steel structure: "hot" analysis

tab. 3.5: Joule losses "hot" model

Flat part $[W]$	Right leg $[W]$	Left leg $[W]$	Overall $[W]$	Silicon $[W]$
4702	76	550	4854	2810

As we can see from the tab. 3.5 Joule losses on steel structure increase of about 53% moving from "cold" to "hot" model.

3.4 Steady State AC Magnetic Models coupling with Transient Thermal

In addition to Steady State AC Magnetic also multi-physics models are done in order to understand especially the thermal behaviour of steel structure.

3.4.1 Materials

The principal observed problem in building this model was the difficulty to get thermal materials properties, such as volumetric heat capacity[1] and thermal conductivity[2] in function of temperature[3]. In particular, it was difficult to find these properties for the typologies of Graphite and Aluminium oxide used. For example, many types of Aluminium oxide exist with a wide range of thermal conductivity that depend on its density. In this case knowing that it is a lightweight Aluminium oxide helped to find these physical characteristics.

tab. 3.6: Electrical and thermal properties of materials

	$\rho(T)$ [Ωm]		μ [/]	$K(T)$ [$\frac{W}{mK}$]		$RCP(T)$ [$\frac{J}{m^3K}$]		γ [$\frac{kg}{m^3}$]
AISI-304	48.5	@50°C	1	6.02	@50°C	3.6×10^6	@20°C	7800
	52.2	@100°C		9.75	@100°C	3.9×10^6	@90°C	
	62.5	@200°C		12.89	@200°C	4.2×10^6	@200°C	
	86.8	@500°C		18.28	@500°C	4.5×10^6	@540°C	
	112.5	@1000°C		25.33	@1000°C	4.9×10^6	@870°C	
Aluminium Oxide	Insulator		1	0.12	@100°C	4.76×10^6		400
				0.13	@400°C			
				0.14	@600°C			
				0.23	@1200°C			
Isostatic Graphite	5×10^{-5} $\alpha = -0.0005K^{-1}$	@20°C		80.5	@50°C	1.7×10^6	@50°C	2250
				80.5	@227°C	2.0×10^6	@227°C	
				63.0	@527°C	3.9×10^6	@527°C	
				47.5	@927°C	6.9×10^6	@927°C	
Felt Graphite	Insulator		1	0.18	@20°C	2.19×10^6		180
				0.20	@500°C			
				0.45	@1250°C			
				0.58	@1750°C			
Copper	0.1564×10^{-7} $\alpha = -0.00427K^{-1}$	@0°C	1	394		3.52×10^6		8920
Silicon (molten)	0.7×10^{-8}		1	460	@1414°C	2.55×10^6	@1414°C	2580

Furthermore, the *i*DSS process takes place in controlled atmosphere, in particular inside the furnace there is Argon at low pressure, so for thermal analysis is necessary to insert also this material. Obviously Argon has the same electrical properties of Air, are specify only thermal characteristics.

[1] RCP: volumetric heat capacity
[2] K: thermal conductivity
[3] f(T)

tab. 3.7: Thermal properties of Argon

	$K(T)$ $\frac{W}{mK}$	$RCP(T)$ $\frac{J}{m^3K}$	γ $\frac{kg}{m^3}$
Argon	0.01772	927.68	1.784

3.4.2 Physics

In this model also thermal interaction between steel structure, Argon and upper susceptor are taking into account. In order to simplify the model these interactions are represented by surface regions having the following characteristics:

- Argon face region: this region imposes convective exchange between Argon and steel structure. From G2.5's tests, the Argon temperature measured was about $150°C$. The convection coefficient, being the pressure very low and the Argon a bad "refrigerant" gas, is imposed of $5\frac{W}{m^2K}$. The purpose of this region is to consider the convective exchanges between steel structure and other parts considered in the model, like molten Silicon, or not considered, like other graphite parts that compose the system.

- Upper susceptor region: this region imposes the temperature of Graphite at $1600°C$ in order to taking into account the heating supplied by the upper inductor. Like the temperature of Argon, this value is coming from G2.5's test. Being this simulation a transient, imposing this temperature since the first step could cause an overshooting and oscillations of initial steps' solutions. In fig. 3.11 this error is more evident for power than temperature behaviour.

  In fact $1600°C$ are too much higher than $20°C$ that is the initial value of temperature hypothesizes by Flux, so the problem for initial steps could be bad posed. For obtaining a correct behaviour of steel structure temperature and power transfered, a linear increasing temperature with a gradient of $150\frac{°C}{h}$ is imposed to the region. With this trick the first steps error doesn't disappear, but decreases a lot. This value of temperature gradient for the upper susceptor comes from the linear interpolation of heating process characteristic showed in fig. 3.12 regarding G2.5 tests.

- Furnace case face region: for taking into account the interaction between steel structure's legs and the furnace case, a face region with imposed temperature of $50°C$ is define.

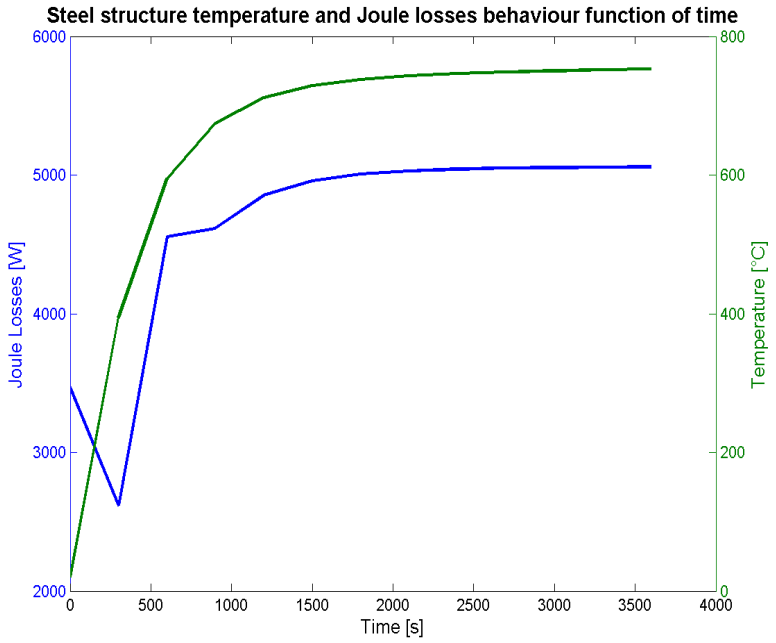

fig. 3.11: Temperature and Joule losses vs Time evaluate from a scenario with wrong time stepping

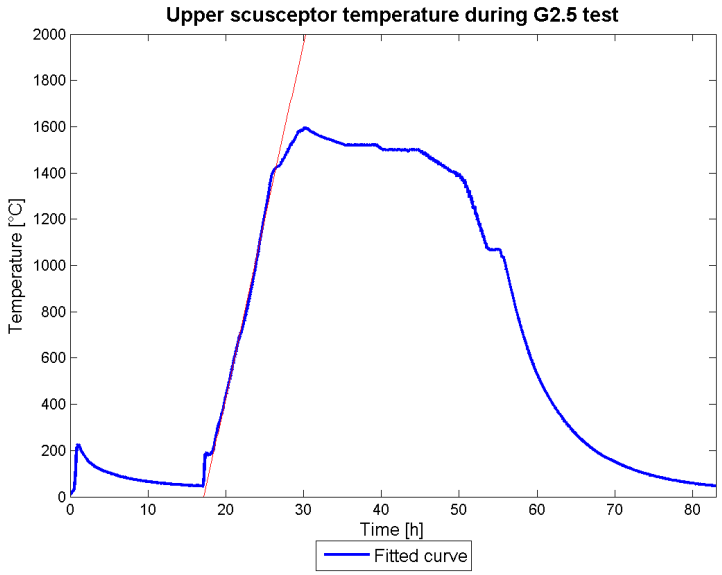

fig. 3.12: Temperature and Joule losses vs Time evaluate from a scenario with wrong time stepping

Before starting with the main solving process, many secondary solution were computed in order to define an ad hoc time scenario for steady state AC magnetic coupled with transient thermal simulations. This study was done, especially, for tuning time steps. In particular, being exponential temperature and power behaviours, the choice of

the time steps at the beginning and during the "knee" transition is crucial for a precise solution. Also a reduced time steps list was applied in order to decrease simulation's time costs[4]: the reducing criteria used concerns on imposing a maximum power gradient of $150\frac{W}{h}$. Also power and temperature behaviours with reduced time steps list are showed in the next section.

3.4.3 Results and Post Processing

To understand the furnace behaviour during the real heating process, the duration of the transient is 10 hours. If it is not specified, the results refer to the complete time steps list simulation.

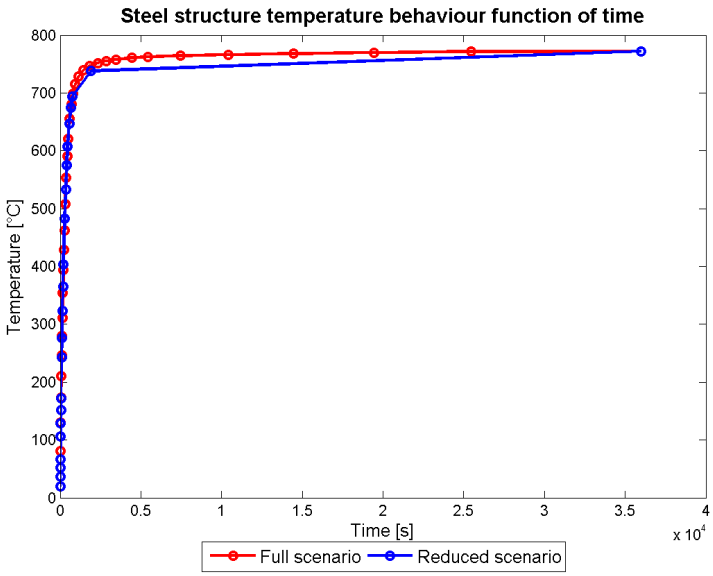

fig. 3.13: Temperature vs Time evaluate from different scenarios

A fixed point inside the steel structure's region is defined for checking the coincidence between temperature behaviour obtained by both steps lists. In fig.3.13 it is possible to compare both behaviours: the initial slope is similar for both scenarios because of the large number of steps in this part; the biggest difference between the two curves is in the knee region, because of the number of point decreases. In general the two curves are similar despite the different number of points. This does not occur instead for power behaviours showed in fig.3.14: the evolution of these curves are substantially differents in the curves' knees. In order to solve this problem and make the two curves similar,

[4]The Steady State AC Magnetic simulation cost is of about one hour

some point could be added in the zone where slope changes.

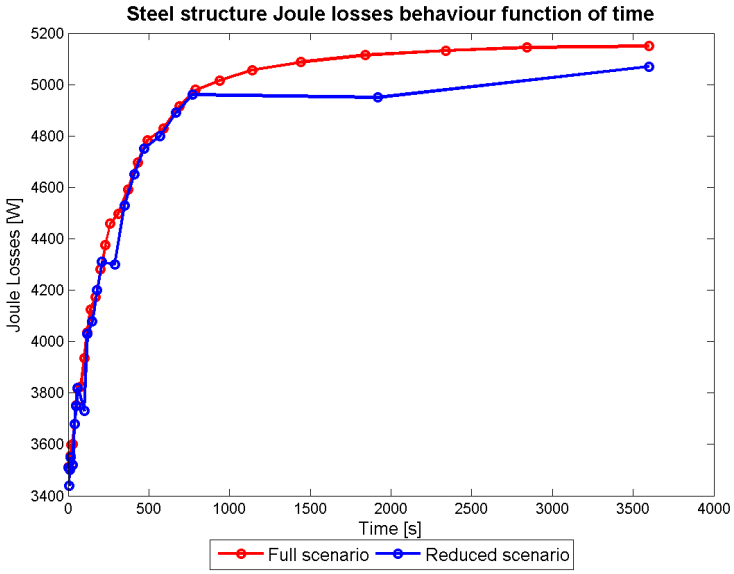

fig. 3.14: Power's vs Time evaluate from different scenarios

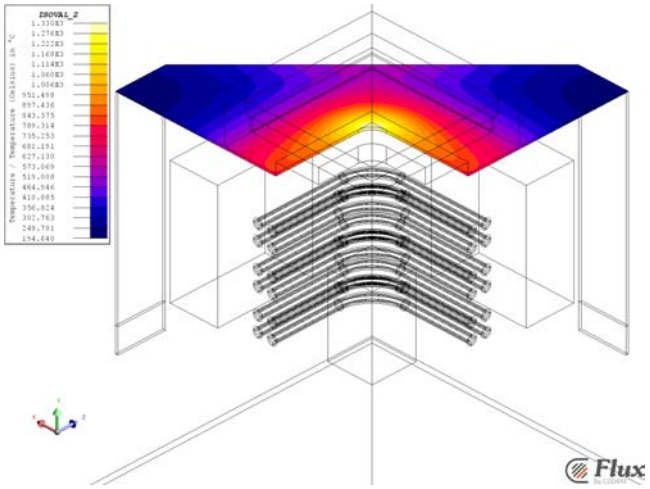

fig. 3.15: Temperature isovalues on steel structure at finished transient

Obviously, the analysis concentrates on regime steel structure temperature distribution. This distribution is shown in fig. 3.15 and it highlights the maximum temperature reached by steel that is about $1300°C$. This temperature is unsustainable for this material: in particular AISI-304 's softening temperature is near $650°C$. So this structure is impossible to use in these conditions due to the high temperature stress induced by the furnace's mode of operations.

This problem is due to the fact that the steel structure was designed without knowing

the real dimensions of lateral inductor. The new "cement-like" structure imposes the necessity to build an inductor larger than expected. So, the magnetic field applied to the steel structure is higher than expected too.
A solution for this problem is needed and it will be the principal goal for this study.

Chapter 4

Numerical design of for G1 furnace

In this chapter, the analysis of the modifications designed for the G1 experiment is presented. Numerical models and preliminary test have demonstrated that the metallic frame that hold the upper susceptor is heated too much by the new lateral inductor. Numerical analysis have been used for study different solutions of steel structure heating problem. The possible solutions concern:

- changes in the lateral inductor circuit;
- place a magnetic shield between steel structure and lateral inductor;
- redesign the steel structure.

In each section, the results of Steady State AC Magnetic simulations are shown. Only "hot" configurations, i.e. configurations with material properties evaluated in hot conditions, are taken into account for understanding the Joule losses in a regime situation.

Best solution's choice is discuss in order to make the furnace usable for the real solidification process. Also, for this configuration the solution of a electromagnetic-thermal-coupled simulation is shown.

4.1 Solution 1

4.1.1 Description

This configuration considers the short-circuit of upper coils of lateral inductor. With this method the magnetic field decreases due the lower number of active coils. Moreover, these short-circuited coils operate like a magnetic shield. As well known, eddy currents

$\boldsymbol{J}$ are connected with magnetic flux density $\boldsymbol{B}$ with Faraday's and Ohm's law; they are exposed on eq.4.1.

$$\begin{cases} \nabla \times \boldsymbol{E} = -\frac{\partial \boldsymbol{B}}{\partial t} \\ \boldsymbol{E} = \rho \boldsymbol{J} \end{cases} \tag{4.1}$$

So, these currents produce a magnetic field in opposition with the one produced by the lateral inductor: this is due to the minus sign in the first equation. In this way, the field concatenated by the steel structure is lower than before.

For evaluating the current density inside the upper coils, they are modelled with solid conductor, instead coil, and they are not connected with any electrical component. With the same goal, the mesh in these coils is tinier than before.

4.1.2 Results

The fig. 4.1 shows the magnetic field in case of short-circuited coils. It is possible to see the shield effect produced by eddy currents inside upper coils. The magnetic field produced by lateral inductor appears pent on the lower part of the model. In this way, the steel structure is interested by a lower field, so there are not huge eddy currents in it (fig. 4.2).

tab. 4.1: Joule losses "hot" model with short-circuited coils

Flat part $[W]$	Right leg $[W]$	Left leg $[W]$	Overall $[W]$	Silicon $[W]$	Coils $[W]$
631	40	321	721	1360	17370

From tab. 4.1 the advantage obtained with respect to the losses on steel structure is clear: they decrease of 85%. Otherwise, the disadvantage of this configuration consists on the great current density inside upper coils as it is shown in fig. 4.3. In fact, Joule losses evaluated on short-circuited coils ($17.4kW$)are too high, the actual cooling system is not able to dissipate them. More over, the electrical "efficiency" of the process decreases because:

- Losses on upper coils are higher in comparison with that one saved on the steel-
- Power transferred to the melt decreases of 52%

In order to avoid these disadvantages, it was thought to realize the short-circuit intermittently, but at the end this solution has been discarded.

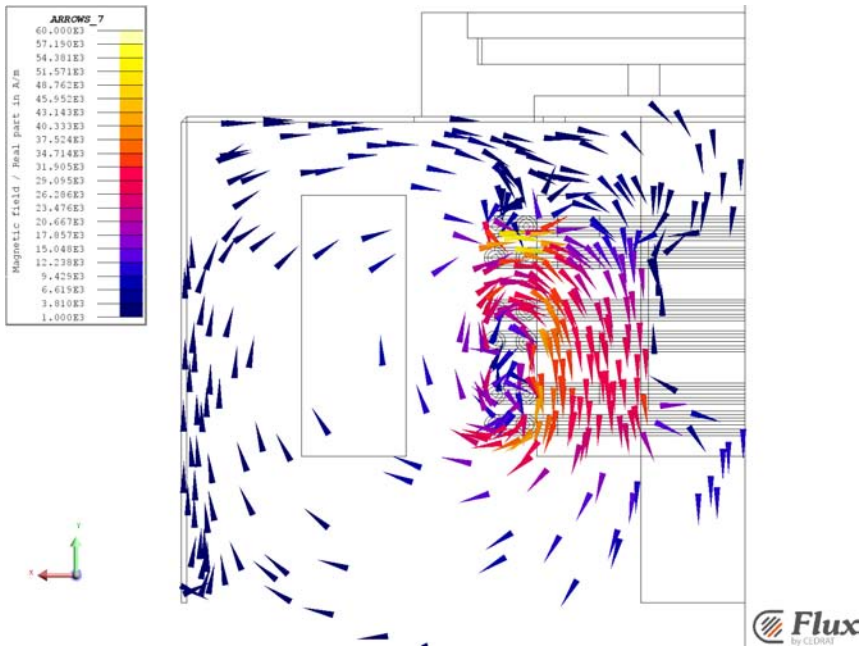

fig. 4.1: Magnetic field with short-circuited coils

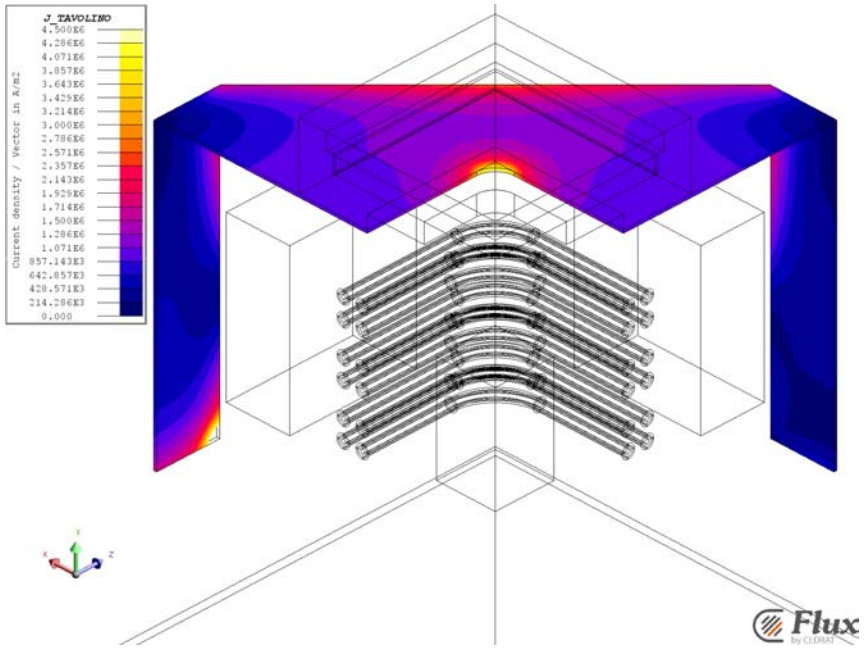

fig. 4.2: Current density distribution in steel structure with short-circuited coils

4.2 Solution 2

4.2.1 Description

The main problem of solution 1 concerns the Joule losses inside the short-circuited coils. For avoiding this issue, I built a model with the upper coils circuit in open circuit

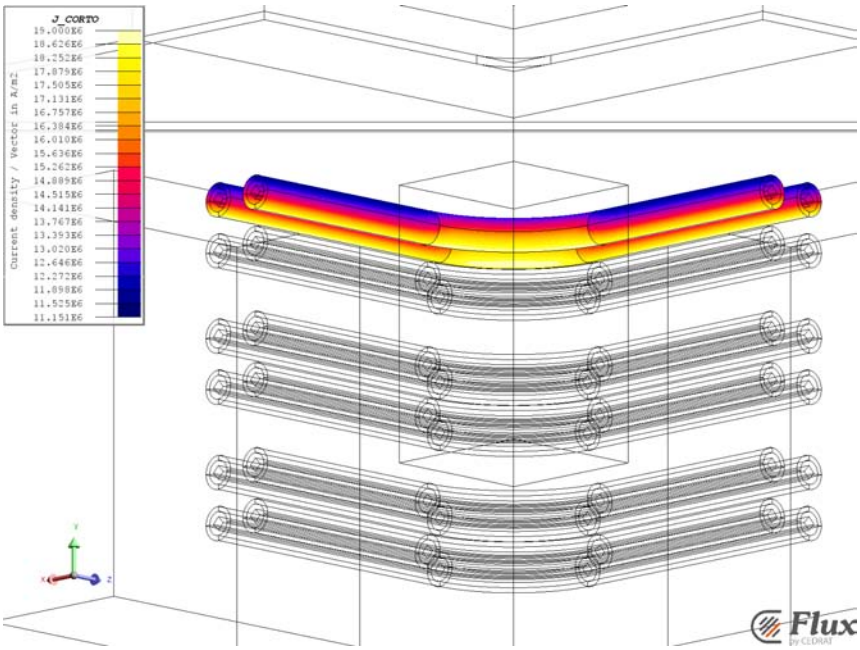

fig. 4.3: Current density distribution in short-circuited coils

conditions. Like the previous solution, the magnetic field produced by lateral inductor decreases. The difference consists in the lighter shield effect produced by eddy currents. In fact, because of the open circuit, in the upper coils there are lower eddy currents than those produced in short circuit conditions. But, in this way, Joule losses on coils could decrease dramatically.

In order to model the open circuit a little air gap is built on a end-connection of coils.

4.2.2 Results

In this case the magnetic field that concatenates the steel structure is higher then the previous case (tab. 4.4). Consequently eddy currents are greater than before (fig. 4.5.

This time, tab. 4.2, Joule losses decrease of 64% respect the starting model. In the upper coils, the losses are quite low so it is possible to use the inductor's cooling system to dissipate them. Also in this case, power transmitted on melt decreases of 25%. In any case, like "short-circuit" solution an intermittently work cycle was proposed.

tab. 4.2: Joule losses "hot" model with no-loaded coils

Flat part $[W]$	Right leg $[W]$	Left leg $[W]$	Overall $[W]$	Silicon $[W]$	Coils $[W]$
1657	44	433	1745	2100	633

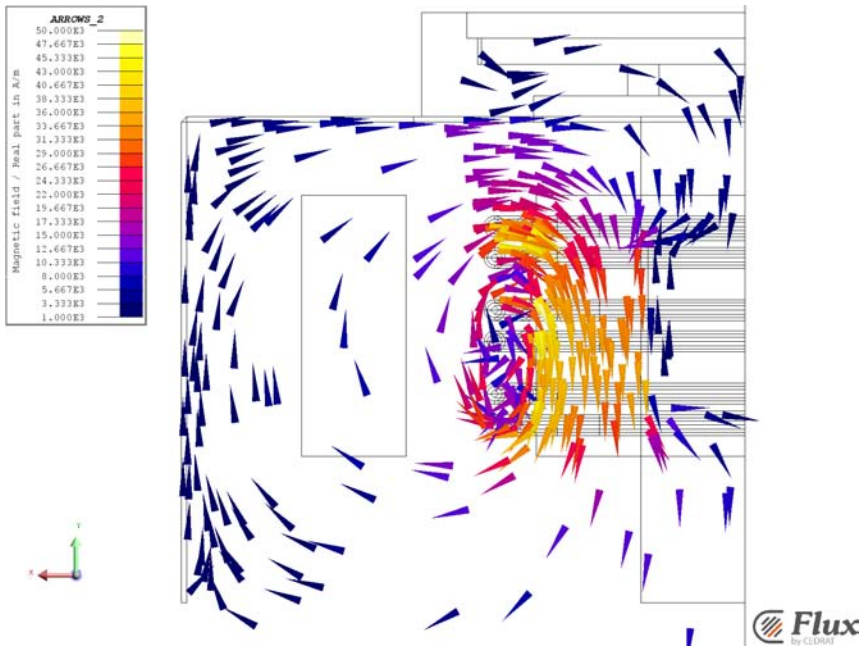

fig. 4.4: Magnetic field in "no-load" configuration

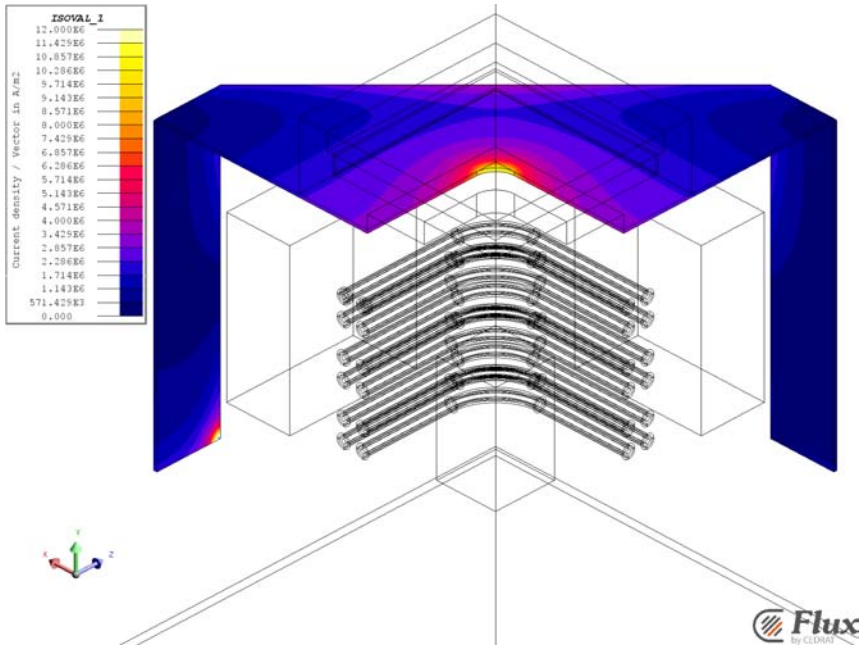

fig. 4.5: Current density distribution in steel structure with open coils

4.3 Solution 3

4.3.1 Description

Taking into account advantages and disadvantages of previous configurations, these are declared unsuitable to solve the heating problem. Also, the control of the converters,

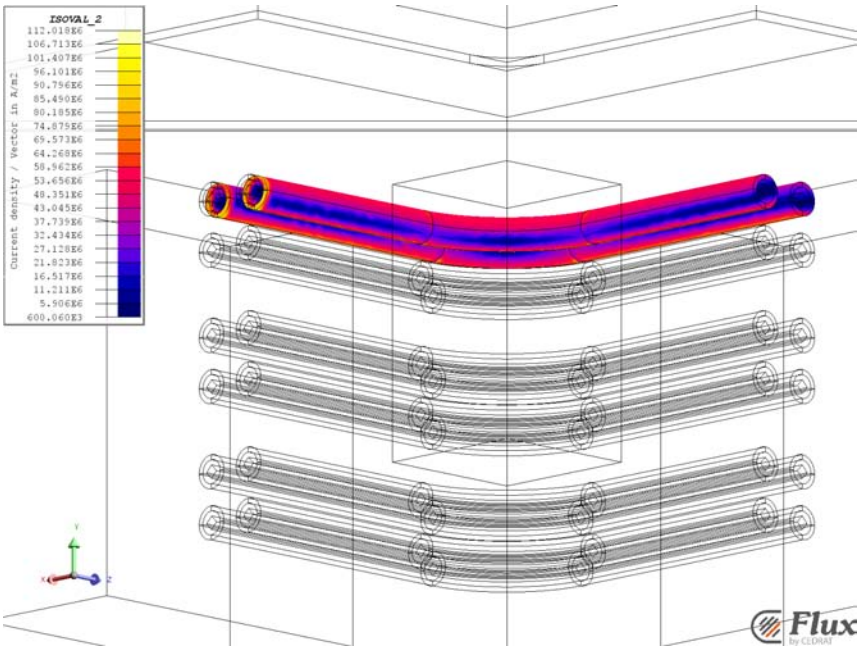

fig. 4.6: Current density distribution in open coils

for the intermittently conditions of operation, should be difficult to implement and realize. The idea to create a magnetic shield effect for the steel structure could be realize in another way: using an high permeability material. The fig. 4.7 shows the geometry used for this simulation.

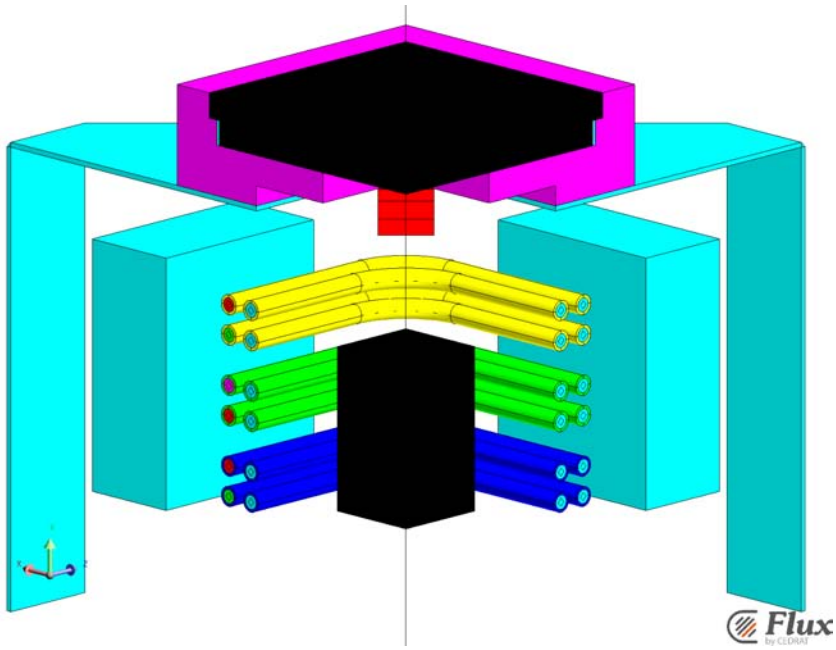

fig. 4.7: Model's geometry with "angular" Ferrite

In this solution, it is proposed to place a block of Ferrite, or a different magneto dielectric material like Fluxtrol50®, under the corner of steel structure's hole. This location is chosen because there is the highest current density. Based on the fixing possibilities, the Ferrite is placed as near as possible to the steel structure: one centimetre under it. This configuration allows the Ferrite to work with lower magnetic field in order to avoid its saturation. By reference to a commercial material, such as Fluxtrol50®, if it works in saturation condition it assumes a lower value of permeability so its effect decreases (fig. 4.8). Moreover, a higher magnetic field means a higher magnetic flux density, so, based on eq. 4.2, the losses on Ferrite increase.

$$P_v = 2.73 f^{1.125} B^{2.5} \quad [\frac{W}{cm^3}] \tag{4.2}$$

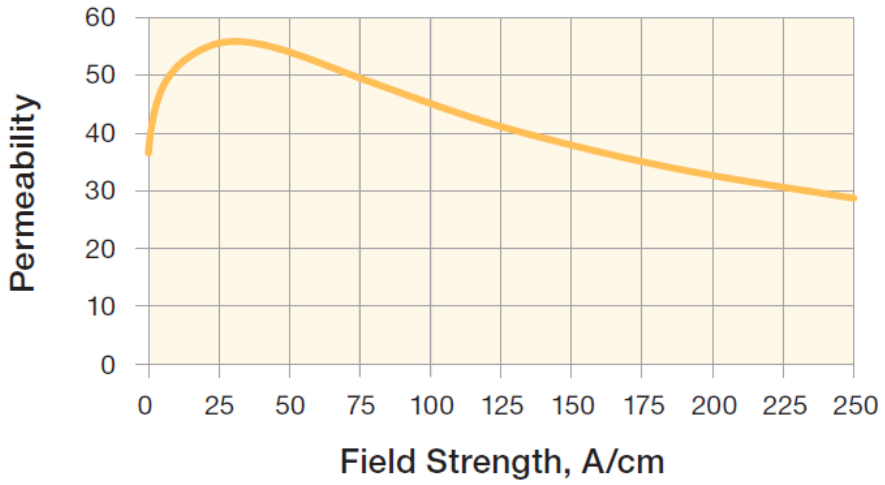

fig. 4.8: BH curve of Fluxtrol50®

Regarding properties of Ferrite, as well known, it is obtained by sintering magnetic powder with a glue that is used, also, for insulate the grains each other. Furthermore, this type of material needs a non-linear model for its analysis because of the saturation. But, for decreasing computational costs, in the model a constant permeability is imposed to Ferrite. In tab. 4.3 Ferrite properties are summarized.

tab. 4.3: Properties of Ferrite

	$\rho(T)$ Ωm	μ $[/]$	$K(T)$ $\frac{W}{mK}$	$RCP(T)$ $\frac{J}{m^3K}$	γ $\frac{kg}{m^3}$
Ferrite	Insulator	50	230	3×10^6	6800

4.3.2 Results

To analyse magnetic field behaviour on Ferrite (fig. 4.9), a "cut plane" (a plane where the FEM software can display the distribution of field quantity)is created by rotating the plane XY of $45°$. Ferrite does not allow the field to concatenate the steel on hole's corner. But, some deflected field lines concatenates the steel outside the zone cover by Ferrite. Eddy currents, represented on fig. 4.10, results to be a little bit lower than previously cases, but another hotspot results along the diagonal. So, if the current intensity decreases, the surface cover by higher eddy currents and, thus, the resistance increase. In fact, Joule losses of steel structure decreases only of 16% in respect to the starting model. The improvement on power transfer to the Silicon is near to 5%.

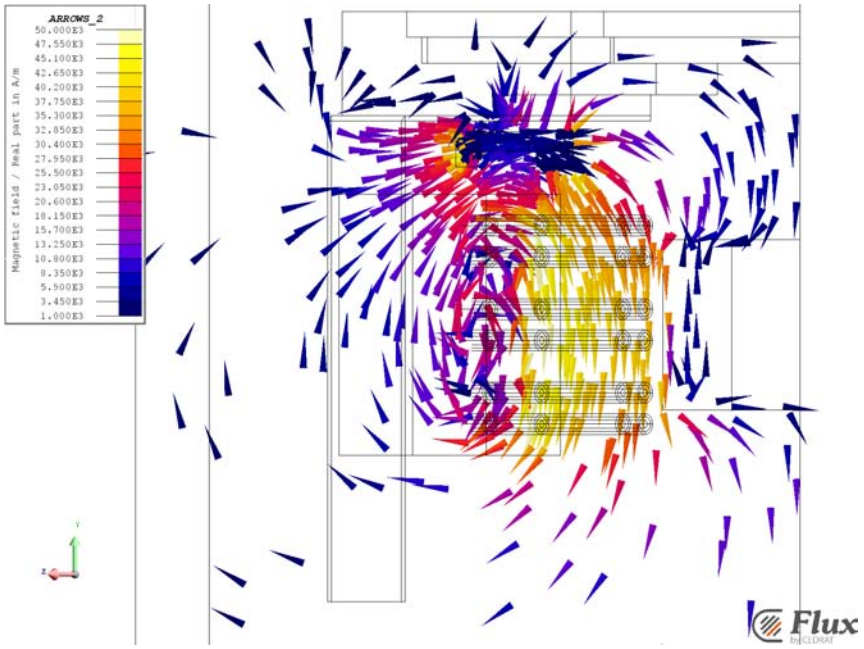

fig. 4.9: Magnetic field on "angular" Ferrite

tab. 4.4: Joule losses of "hot" model with "angular" Ferrite

Flat part $[W]$	Right leg $[W]$	Left leg $[W]$	Overall $[W]$	Silicon $[W]$
3942	72	570	4086	2939

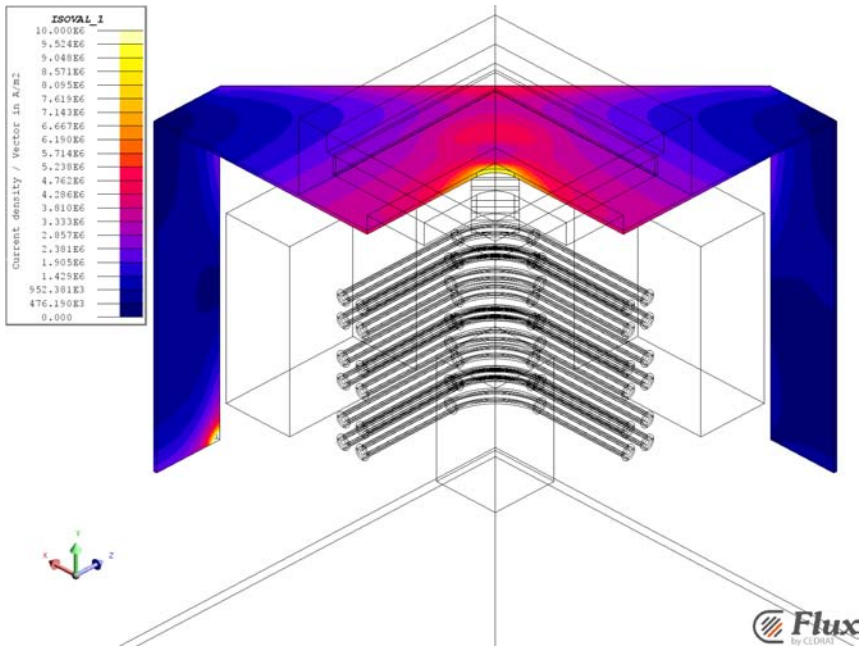

fig. 4.10: Current density distribution in in steel structure with "angular" Ferrite

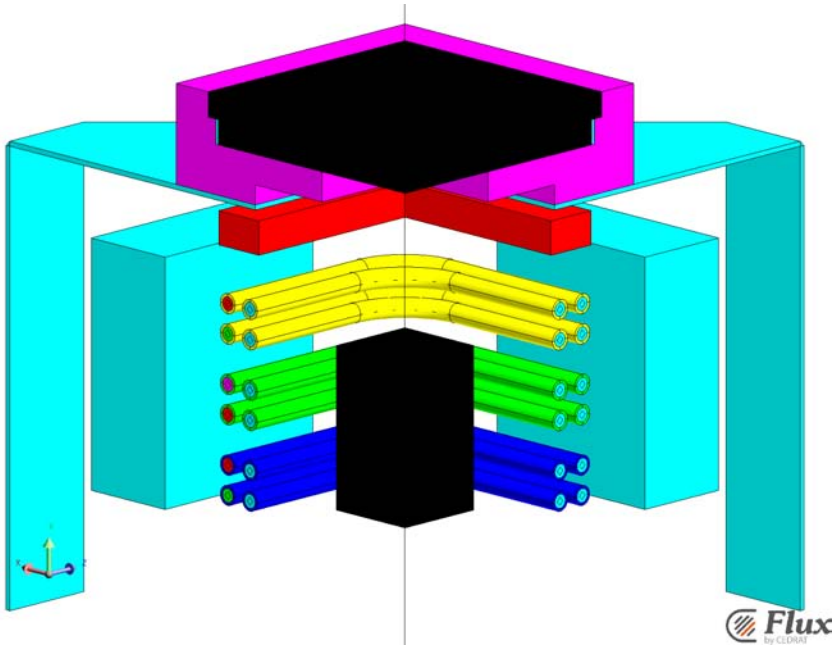

fig. 4.11: Model's geometry with "circular" Ferrite

4.4 Solution 4

4.4.1 Description

Trying to improve the effects of Ferrite, it is substituted by a new one. This new piece of Ferrite has the same shape of the inductor, and the same cross section of the

previous one. It is possible to see the new geometry in fig. 4.11.

4.4.2 Results

Respect to the starting configuration, this allows to decrease Joule losses of 27% on steel structure and an increase of power transferred to the Silicon of 11%.

tab. 4.5: Joule losses of "hot" model with "circular" Ferrite

Flat part $[W]$	Right leg $[W]$	Left leg $[W]$	Overall $[W]$	Silicon $[W]$
3414	74	597	3562	3127

Now, the behaviour of field lines is the same for symmetry and cut plane. So, for current density distribution on steel, similarly to the "angular Ferrite", the intensity decreases and the interested surface increases again, fig. 4.13. A sort of current "circle" is present, it is due to the field lines deflected by the Ferrite along all its profile.

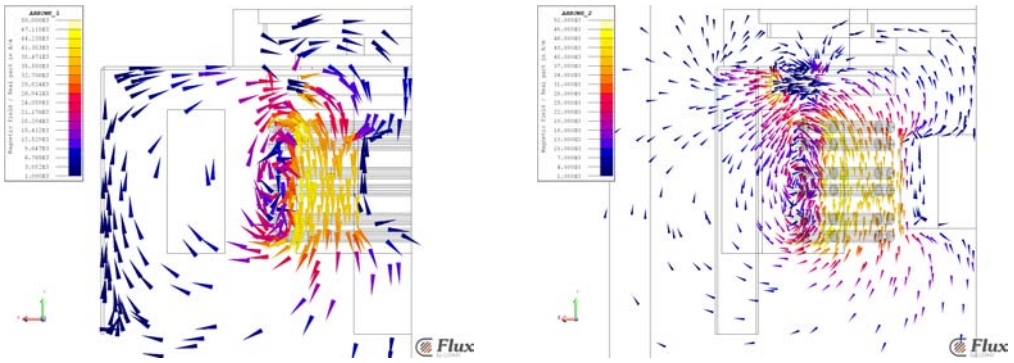

(a) Symmetry plane (b) Cut plane

fig. 4.12: Magnetic field on cut plane and symmetry plane with "circular" Ferrite

4.5 Solution 5

Solutions regarding electrical circuit and magnetic shield were discussed before. Now, new geometrical configurations for steel structure are treated.

4.5.1 Description

The principal problem of the configurations analysed so far is the closed path followed by currents. Essentially, the structure works like a short circuited coil. So, a

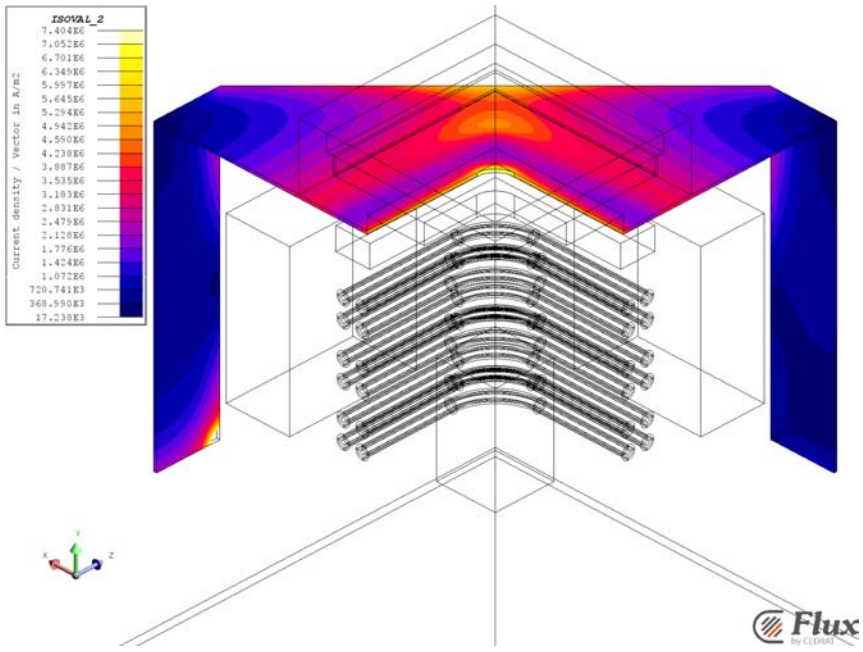

fig. 4.13: Current density distribution in in steel structure with "circular" Ferrite

solution for this problem could be to cut this path. For doing this, the structure is split in two with a cut of $4mm$ from the hole's corner to the middle of the external side. A problem of this configuration could be the difference of potential induced by the new air gap. All the steel parts are connected to the vessel that works like the ground potential. Ultimately, the eddy currents induced in the steel should not create a difference in potential such to lead to the discharge into the air gap. Anyway, another useful modification could be enlarging the hole, but it is not considered in this configuration.

4.5.2 Results

The fig. 4.14 shows eddy currents distribution and its path with the new geometry. It is possible to see that currents do not follow a close path around the hole like before. In particular, they follow a close path inside their structure's sector, so their intensity decrease. Note that the current direction on cut's edges is in opposition. This behaviour causes the partial cancellation of the currents in that zone. Also, with fig. 4.14(b) it is possible to see that the surface interested by eddy current is smaller than before. These considerations lead to the Joule losses resumed in tab. 4.6.

The overall losses are evaluated multiplying for two the losses on right leg and right flat part. This is for avoiding problems connected to the abnormal current distribution on left leg showed before. The table shows that Joule losses on steel structure decrease of 85% and increase of 20% on the molten Silicon. So, this configuration leads to losses

those are sustainable by the steel, hence it could be a good solution.

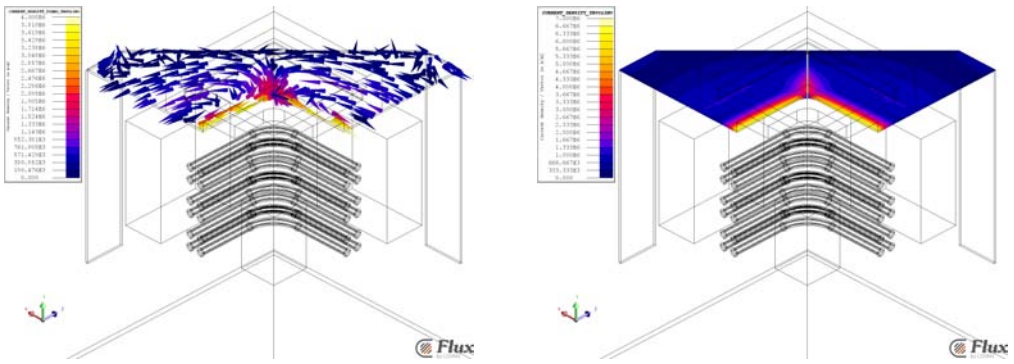

(a) Arrows (b) Isovalues

fig. 4.14: Current density on split steel structure

4.6 Solution 6

4.6.1 Description

The possibility to change the entire steel structure was taken into account. The new structure is composed by four brackets that could be obtained by cutting the initial "table" configuration. The "leg's" height and width remain the same, whereas the length of horizontal part is decrease. In this way, the magnetic field lines intensity concatenated by the steel is lower. The geometry resulted by these changes is shown in results section on fig.4.15. This configuration should not lead to a weaker mechanical structure.

4.6.2 Results

From fig. 4.15(b) it is possible to see that current density does not exceed $2.7\frac{A}{mm^2}$. Also, the region interested by eddy currents is smaller than before. The Joule losses obtained by this simulation are shown in tab. 4.7.

Thus, the overall losses are approximately zero (98% less than starting model) and the power transferred to the melt increase of 20%.

tab. 4.6: Joule losses of "hot" model with split steel structure

Right flat part $[W]$	Left flat part $[W]$	Right leg $[W]$	Left leg $[W]$	Overall $[W]$	Silicon $[W]$
336	335	32	712	735	3373

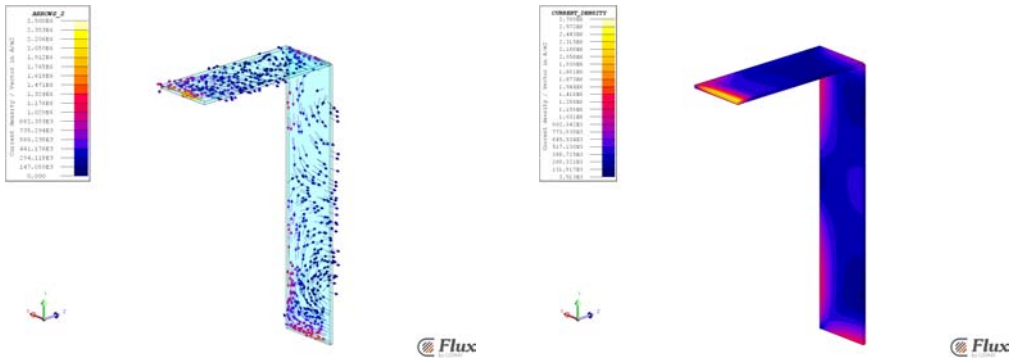

(a) Arrows (b) Isovalues

fig. 4.15: Current density on new steel structure

4.7 Choice of the new configuration

The results in terms of losses are summarized in tab. 4.8. Based on tab. 4.8, the best solution for this problem is to use the steel brackets. So, the advantages of this solution are:

- Minimization of Joule losses on steel structure.
- Maximization of power transferred to the Silicon

These considerations lead to an efficiency improvement. Otherwise, the main disadvantages consists to the mechanical structure weakening. But, this is compensated by the brackets those sustain the lateral inductor. Note that another good solution could be the "split structure" configuration.

For the chosen solution, the results of thermal coupled simulation are shortly exposed. In fig. 4.16 it is showed the behaviour of Joule losses inside the right bracket. It is possible to see that the losses do not exceed the value find on the "hot" model solution. The temperature distribution on the bracket at regime is showed on fig. 4.17.

tab. 4.7: Joule losses of "hot" model new steel structure

Right leg $[W]$	Left leg $[W]$	Overall $[W]$	Silicon $[W]$
48	721	96	3376

tab. 4.8: Joule losses of "hot" model new steel structure

		"Hot" model	Solution 1	Solution 2	Solution 3	Solution 4	Solution 5	Solution 6
Overall	$[W]$	4854	721	1745	4086	3562	735	96
Silicon	$[W]$	2810	1360	2100	2939	3127	3373	3376

The maximum temperature reached is of $265°C$, that is much lower than the softening temperature. Also, in the hotter zone the bracket could exchange with the furnace vessel (not considered). In light of what it is shown up, compare "hot" models to choice the best solution of the overheating problem was correct.

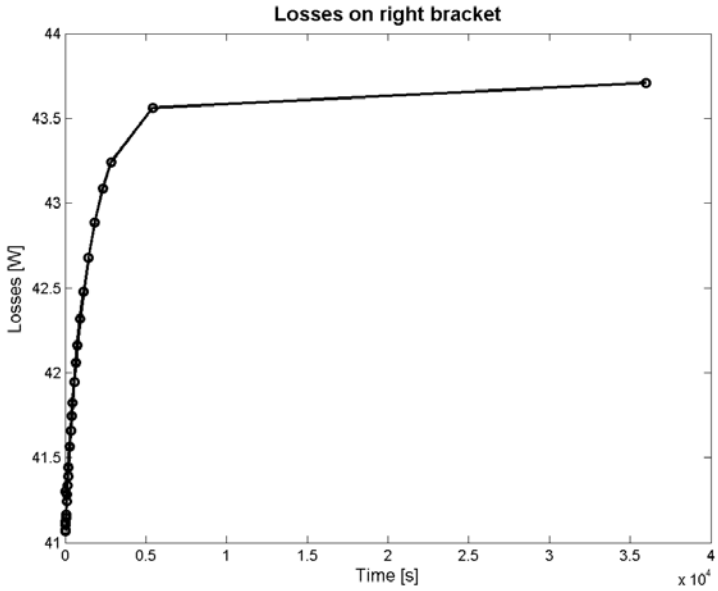

fig. 4.16: Behaviour of losses on steel bracket

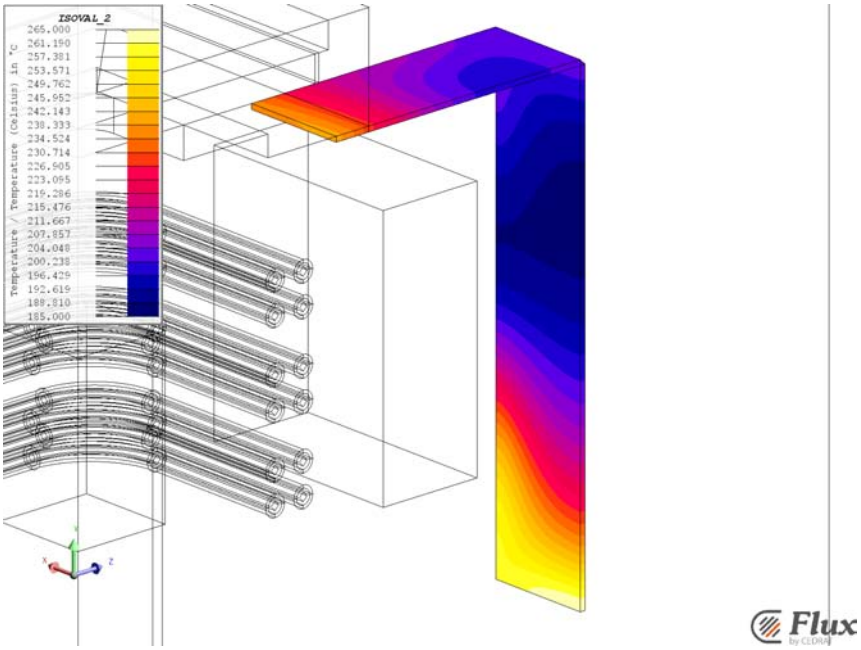

fig. 4.17: Temperature distribution on steel bracket at regime

Chapter 5

Experimental tests

Some, the experimental tests, have been carried on the furnace modified for the G1 experiment, also to verify numerical results. The tests concern:

1. Definition of the converter resonance characteristics.
2. Temperature measurement on original steel structure with open vessel and different configuration.
3. Temperature test on the new steel structure.

5.1 Converter "no-load" resonance characteristic

The new lateral inductor is composed by three groups of four coils. These three groups are supplied by a three-phase current for creating the travelling magnetic field responsible of the stirring. The new converter is able to superimpose to this three-phase current a single-phase one. In particular, for the single-phase current all the coils result to be connected in series. This characteristic describes the current intensity, flowing into the lateral inductor, as a function of the MF frequency. In this case, "no-load" means that the measure is done without the load, i.e. the molten Silicon. Also, this test has been done for both the configurations of the sustaining system.

The converter's interface permits to control the frequency, so a current measure is needed. For measuring the current, flowing into the lateral inductor, an oscilloscope with a Rogowski's probe was used. In order to determine the characteristic, we started with a low frequency and then it is increased as long as the IGBT's protections do not intervene. A similar method is used for finding the right side of the characteristic, we started with an high frequency and then it is decreased. The curves founded are shown in fig. 5.1.

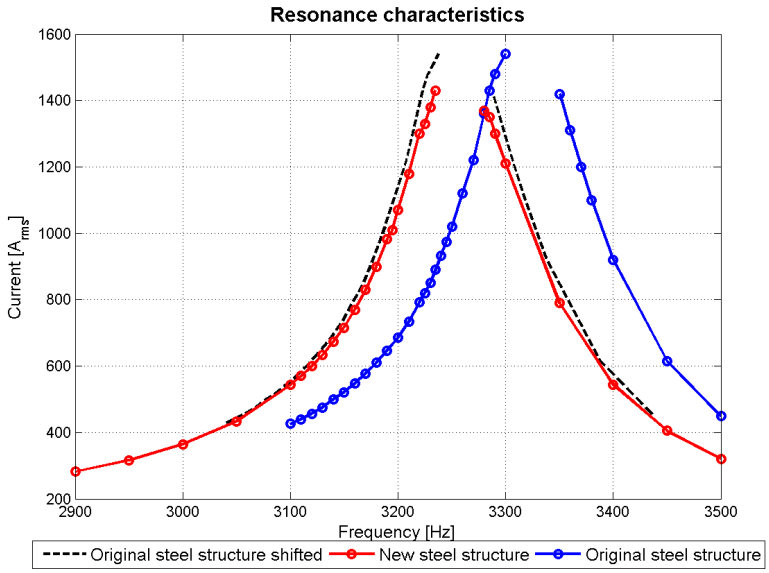

fig. 5.1: Resonance characteristic of the converter

It is possible to do the following observation:

- The converter has to work on the left side of the characteristic. This is due to the higher slope of the right side and for its non well known behaviour. In fact, in this part there is a point of anti-resonance and its position is unknown.

- The resonance frequency, passing from the old to new structure, is shifted to the left, so it decreases. Since it is possible to write the resonance angular frequency with eq. 5.1. This means, given that the matching capacitance is constant, that the inductance increase.

$$\omega_0 = \frac{1}{\sqrt{LC}} \tag{5.1}$$

- Unfortunately, it is impossible to do some quantitative consideration regarding the resistance "seen" by the converter: it could be possible knowing the current peak at ω_0. But, shifting the blue curve over the red one (black discontinuous), it is possible to see that the resistance changes.

- Obviously, the converter sees values of resistance and inductance different than during the normal work. Anyway, this test is useful to know the qualitative behaviour of the $f - I$ characteristic.

During this test section, was analysed the double frequency mode of operation. In particular, it was done a spectrum analysis by FFT[1] tool. This study permits to find the

[1]FFT: Fast Fourier Transform

different frequency modulated by the converter. In particular, it is possible to evaluate the frequency modulated in order to create the travelling magnetic field. In fig. 5.2 shows the overall waveform measured.

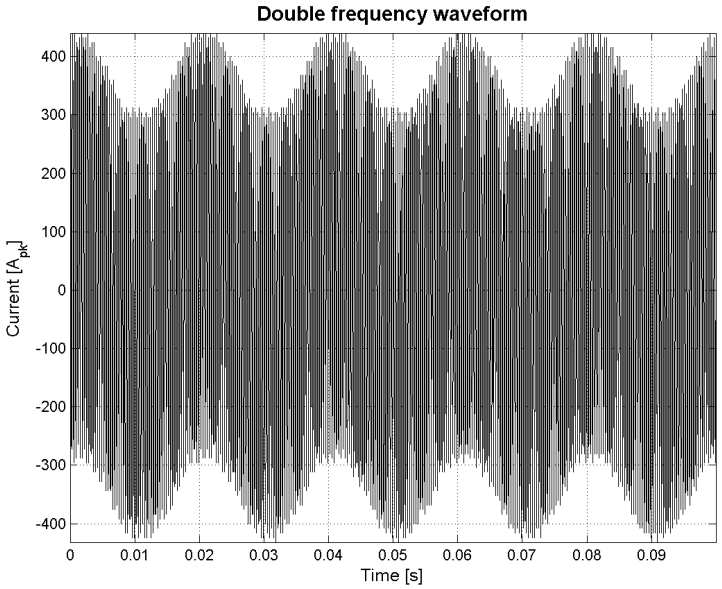

fig. 5.2: Double frequency waveform

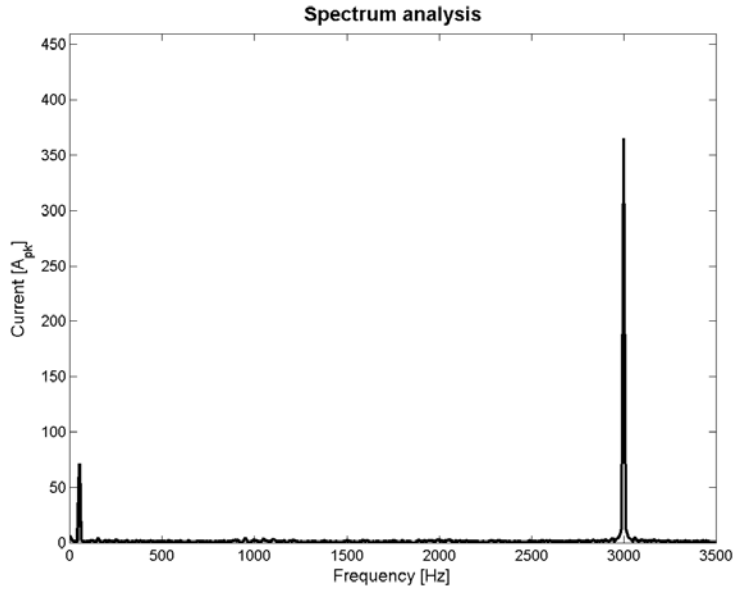

fig. 5.3: Spectrum analysis

It is possible to see the current in one of the three phases at low frequency. This waveform is obtained by the modulation of a single-phase current at high frequency. The frequencies and their corresponding values of current are show in fig. 5.3. The

main frequencies are $20Hz$, $70Hz$ and $3020Hz$. The $3020Hz$ component corresponds to the heating frequency. Otherwise, $20Hz$ and $70Hz$ correspond to the stirring frequency. Maybe, it is possible to distinguish two different low frequencies because of the modulation of a three-phase current with a single-phase current.

5.2 "No load" test

The object of this test is the temperature reached by the steel structure during the "no-load" operation. The temperature is measured in the located hotspot along the diagonal from the hole's corner to the middle of external side. Precisely, the thermocouple is placed $45mm$ far from the corner. These tests are made with a current of $350A$ at the MF frequency of $3kHz$. Also, during the test, it was necessary to turn off the lateral inductor for measuring the temperature. In fact, the thermocouples is subject to the magnetic field and it gave a signal affected by noise. For avoiding this could be useful employ optic fibre to measure the temperature.

To compare the experimental results with numerical data, a new simulation has been done. The model made for the thermal coupling analysis, showed in chap. 3, has been modify. The face region that took into account the thermal to describe the exchanges with Argon at $150°C$ has been changed. Now, a new face region exchanges with Air at $20°C$ using a convection coefficient of $5\frac{W}{m^2K}$. Also, the imposed temperature on upper susceptor faces is deleted; only Joule losses due to eddy currents produced by lateral inductor are take into account.

tab. 5.1: Properties of Air

	$K(T)$ $\frac{W}{mK}$	$RCP(T)$ $\frac{J}{m^3K}$	γ $\frac{kg}{m^3}$
Air	0.026	1200	1.2

The fig. 5.4 shows the temperature behaviour evaluated with measure and numerical simulation. Until 2000 seconds the curve of numerical data follows the experimental data. The two curves seem to diverge in the last part. With a long duration test this behaviour could be verified. Actually, it was difficult to do long tests because the cooling system was insufficient to cool down the cables. Taking into account all the hypothesis done in order to simplify the model, this correspondence between numerical and experimental data means that the numerical model describes rather good the reality. So, this suggests that the numerical results obtained so far are almost correct.

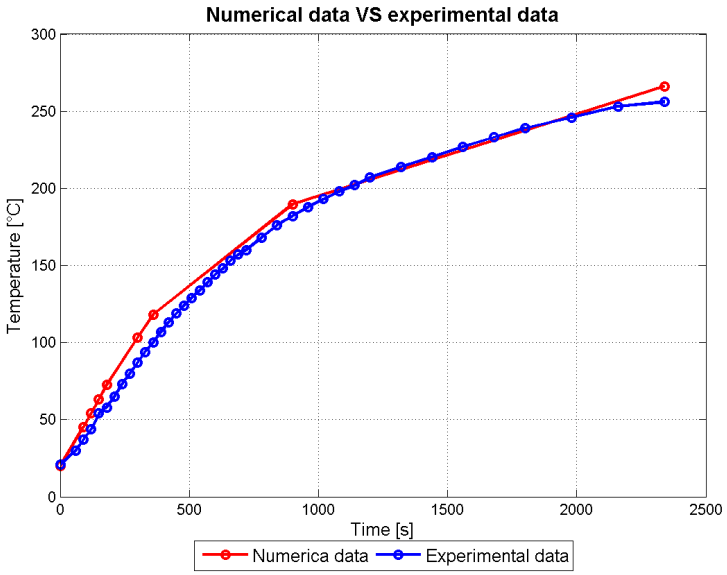

fig. 5.4: "No-load" case: comparison between experimental and numerical data

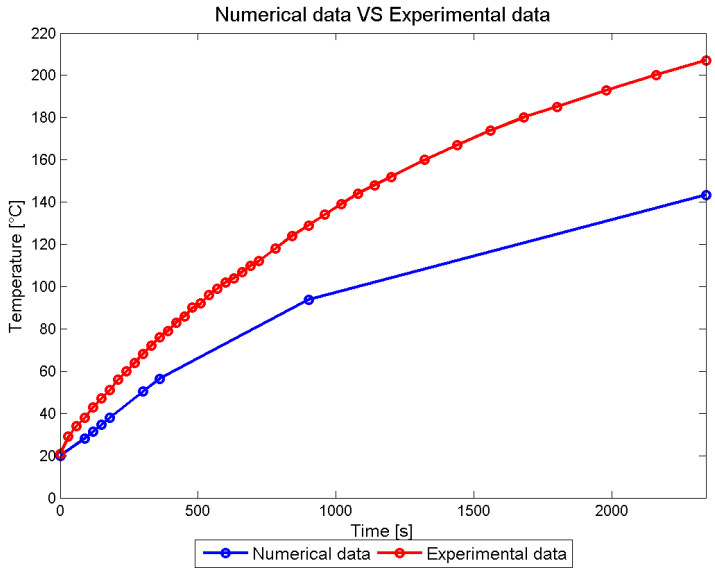

fig. 5.5: "No-load" with Ferrite case: comparison between experimental and numerical data

5.3 "No load" test with Ferrite

This test is done for understanding if the model built up with the "circular" Ferrite describes correctly the reality. The experimental test for this configuration is very similar to the previous one. The only difference consists in the magnetic shield created by the Ferrite blocks. In fact, the geometry of Ferrite proposed in chap. 4 is recreated using

several blocks of Fluxtrol®, available in LEP. So, the overall Ferrite was placed over the lateral inductor at the distance of $20mm$. In addition to the thermocouple on the steel structure, a new one is placed on the Ferrite corner for monitoring its temperature.

Regarding numerical test, the model built up is, again, very similar to the one proposed in chap 4. In this case, the difference concerns the dimension of the overall block of Ferrite: in particular, the actual dimensions are measured and applied to the model.

The comparison between the behaviours of temperature on steel structure of numerical and experimental tests is shown on fig. 5.5. The behaviour of the temperature evaluated with the numerical model is different from the one measured during experimental tests. This difference is due to the difficulty to modelling the Ferrite in the right way. In fact, the typology of Ferrite, Fluxtrol® manufactures different types of magneto dielectric materials, and its magnetic and thermal properties are unknown. So, more accurate data could be reached with the knowledge of the typology of Ferrite and with a non-linear numerical model.

5.4 "No load" test with new steel structure configuration

The simulations presented in chap. 4 gave us the more realistic solution of the heating problem. The geometry of steel structure has been modified in order to obtain four brackets. In this case, the measures are needed for verify the improvement that occurs with the new solution.

In this case, the test is subdivided in two parts. The first preliminary measure consists to check if the four brackets are heated in the same way. For doing this, four thermocouples are placed between the Aluminium oxide support and the brackets. After, the system is heated up with the same values of current and frequency used before until $30°C$. The maximum temperature is setted at $30°C$ because, otherwise, with a higher temperature, the cooling time would be too long. During this transient, taking into account the errors, all thermocouples measured the same temperature. So, the thermal behaviour is the same for all brackets.

In the second part, the measures were focused on a single bracket. Two thermocouple (T1 and T2) are placed on the vertical part of the bracket, at different height. Whereas, other two thermocouple (T3 and T4) are place on the horizontal part, under the Aluminium oxide support. The measures of these thermocouples are shown in fig. 5.6.

The fig. 5.6 highlights that the temperatures measured on the vertical part are going

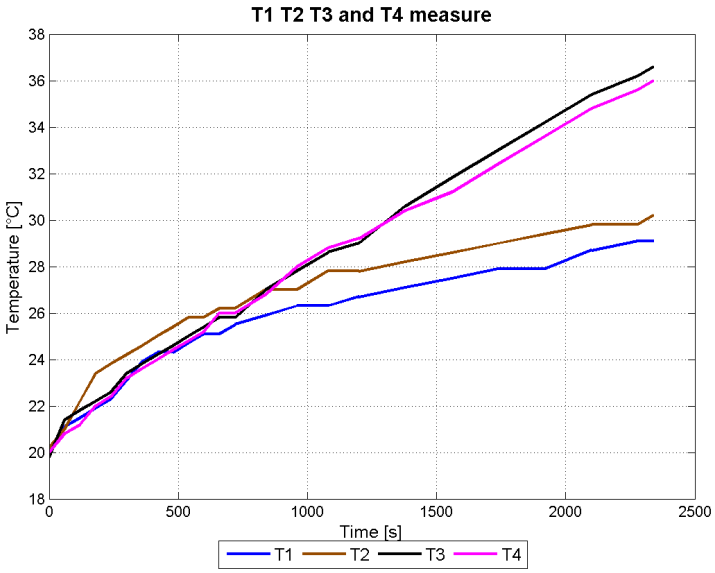

fig. 5.6: "No-load" with new structure case: experimental data

to reach the regime value, the slope decreases quickly. Otherwise, the temperature of horizontal part still increases. So, for understanding the complete behaviour of the temperature, a long duration test is needed. However, the temperatures reached by T3 and T4 are much lower in comparison to the ones reached with the starting geometry.

Conclusions

The main objective of this thesis has been the analysis of the new G1 configuration of the *i*DSS furnace, available in LEP, by means of finite elements method simulations. The first part of the work focuses on the analysis of stirring and heating process of Silicon inside the furnace. From the analysis of heating process, it is observed an issue caused by the power losses due to the eddy currents in the steel structure. Then, we focused the attention on the definition of some solutions to limit the overheating of the new holding system. With Steady State AC Magnetic simulation, it was seen that the Joule losses are too high. Coupling these electromagnetic simulations with the thermal problem, we found unsustainable temperature for AISI-304 corresponding to these values of losses.

Joule losses $[W]$	Maximum temperature $[°C]$	Softening temperature $[°C]$	Fusion temperature $[°C]$
4854	1330	650	1400

Many solutions have been implemented in order to reduce the losses on the steel structure. For all these new configurations, electromagnetic simulations have been done in order to evaluate their effectiveness.

		"Hot" model	Solution 1	Solution 2	Solution 3	Solution 4	Solution 5	Solution 6
Overall	$[W]$	4854	721	1745	4086	3562	735	96
Silicon	$[W]$	2810	1360	2100	2939	3127	3373	3376

From technical and numerical observations, to limit the losses in the steel, it has been chosen to modify the structure geometry in order to obtain four "L" brackets, cutting the initial stainless steel "table". For this solution, also magneto-thermal coupled problem has been solved for evaluating, in numerical way, the new values of temperature reached by the steel (maximum $265°C$).

During all the phases of the work, many experimental measures have been done: measurements were useful both for thesis and for technical-practical solutions. The

measures done on the converter are exposed, in particular the $f - I$ characteristic and how it changes with different configurations of the mechanical structure. One of the main objective of these measures was to evaluate the effectiveness of numerical models. It is possible to say that with quite "simple" model, such as the initial one, numerical results are in good agreement with the experimental ones. Unfortunately, with the addition of complex components, such as Ferrite, the numerical results are less coherent with the experimental measures.

The possible developments of this thesis could be the following:

- Complete the analysis of the new configuration G1: with the addition of all furnace components.
- Exploit magneto-thermal-fluid-dynamic simulations of molten Silicon: until now, all fluid-dynamics analysis for SiKELOR project were done by another partner, the University of Greenwich. It could be useful to start to do this kind of simulations internally to the LEP. This could permit to improve the "know-how" regarding the entire process of multi-crystalline Silicon production.
- Do a test of the complete process of recycling: this permits to compare the final products obtained with the different configurations and verify the improvement of the process.

Bibliography

[1] Czochralski process.

[2] Datasheet of Fluxtrol50®.

[3] Float zone crystal growth.

[4] Matweb: material property data.

[5] F. Dughiero, M. Forzan, N. Sempreboni, and A. Tolomio. Effects of superimpose low and medium frequency magnetic fields in induction direction solidification system.

[6] Sergio Lupi. *Fundamentals of Electroheat*.

[7] V. Rudnev, D. Loveless, R. Cook, and M. Black. *Handbook of Induction Heating*.

[8] Peter Rudolph. Travelling magnetic field applied to bulk crystal growth from the melt: the step from basic research to industrial scale.

[9] Julius Adams Stratton. *Electromagnetic Theory*.

[10] S. Taniguchi, N. Yoshikawa, and K. Takahashi. Application of EPM to the separation of inclusion particles from liquid metal.

[11] Alessandro Tolomio. Simulazioni numeriche per lo sviluppo di tecniche innovative di casting per la produzione di SoGSi nel sistema iDSS.

[12] Manuel Zordan. Design of iDSS control system using Siemens PLC S7 300.